

Nightside Pi2 wave properties during an extended period with stable plasmopause location and variable geomagnetic activity

M.D. Hartinger¹, S. Zou², K. Takahashi³, X. Shi¹, R. Redmon⁴, J. Goldstein⁵, W. Kurth⁶,
J.W. Bonnell⁷

¹Department of Electrical and Computer Engineering, Virginia Tech, Blacksburg, Virginia, USA.

²Department of Climate and Space Science and Engineering, University of Michigan, Ann Arbor, Michigan, USA.

³Applied Physics Laboratory, Johns Hopkins University, Laurel, MD, USA.

⁴National Oceanic and Atmospheric Administration, Boulder, CO, USA.

⁵Southwest Research Institute, San Antonio, TX, USA.

⁶Department of Physics and Astronomy, University of Iowa, Iowa City, Iowa, USA.

⁷Space Science Laboratory, University of California, Berkeley CA, USA.

Key Points:

- Plasmopause location stable before, during, and after this substorm over wide range of MLT
- Multiple intensifications of a plasmaspheric virtual resonance (PVR) with spatially varying amplitude
- PVR wave frequency remains stable at 8.2+/-0.53 mHz during two hour period despite changing magnetospheric and ionospheric conditions

This is the author manuscript accepted for publication and has undergone full peer review but has not been through the copyediting, typesetting, pagination and proofreading process, which may lead to differences between this version and the [Version of Record](#). Please cite this article as doi: [10.1002/2017JA024708](https://doi.org/10.1002/2017JA024708)

Corresponding author: Michael D. Hartinger, mdhartin@vt.edu

Abstract

The frequencies and amplitudes of inner magnetosphere Pi2 waves are affected by the radial plasma density profile. Variable geomagnetic activity and external driving conditions can affect both wave properties and density profiles simultaneously. When interpreting observations, this can lead to ambiguity about whether changing wave properties are due to changing external conditions, density profiles, or a combination of factors. We present a case study using multi-point ground-based and in situ measurements to examine Pi2 wave properties during a period of variable geomagnetic activity. Multiple satellite passes demonstrate the density profile and plasmopause location is stable for at least two hours over a wide range of MLT. This stability allows us to examine how factors besides the radial density profile affect Pi2 wave properties. We find evidence for Pi2 waves with a broadband frequency spectrum as well as a discrete frequency plasmaspheric virtual resonance (PVR) that is observed at low, mid, and high-latitudes and both inside and outside the plasmopause. The PVR is excited in repeated bursts before, during and after (1) the development of a substorm, (2) several auroral intensifications, (3) the development of Sub-Auroral Polarization Stream (SAPS) flows/electric fields/conductivities, and (4) variable Interplanetary Magnetic Field (IMF) conditions. Through all these changes the PVR frequency remains remarkably stable (8.2 ± 0.53 mHz, based on low latitude ground magnetometer observations), suggesting these variations have little effect on the frequency. This is consistent with PVR model predictions for a stationary plasmopause.

1 Introduction

Ultra Low Frequency (ULF) waves in the Earth's magnetosphere are classified according to their frequencies and durations [Jacobs *et al.*, 1964]. Pi2 waves have periods of 40-150 s (7-25 mHz) and occur during events lasting roughly 10-15 minutes; they are primarily a nightside phenomena [Keiling and Takahashi, 2011]. Models of Pi2 waves often describe wave dynamics using a magnetohydrodynamic (MHD) approximation [e.g., Lee and Kim, 1999; Fujita and Tanaka, 2013; Lysak *et al.*, 2015; Ream *et al.*, 2015].

Models and observations show that many ULF wave modes are strongly affected by the radial Alfvén speed profile [e.g., Kivelson *et al.*, 1984; Hartinger *et al.*, 2010; Archer *et al.*, 2015, 2017]. In the inner magnetosphere, variations in the total magnetic field are often small compared to background values while density variations can be significant; thus, when considering Alfvén speed variations and ULF wave properties in the inner magnetosphere, constraining the radial density profile is crucial.

The plasmasphere - a region of cold, dense plasma in the inner magnetosphere - often creates conditions favorable for the trapping of MHD wave energy. Several Pi2 models predict eigenmodes similar to radially standing MHD fast mode waves with frequencies primarily determined by the radial density and Alfvén speed profiles [e.g., Lee and Kim, 1999]. For example, plasmaspheric virtual resonances (PVR) have similar polarizations to radially standing fast mode waves (i.e., azimuthal electric field and field-aligned magnetic field 90 degrees out of phase), radially distributed nodes and anti-nodes, and stable frequencies over a wide range of latitudes (L values) and longitudes. In many cases, signals measured at widely separated latitudes and longitudes exhibit little or no phase shift, indicating globally coherent wave activity with very small azimuthal wave numbers [Li *et al.*, 1998; Nosé *et al.*, 2006]. PVR can also have finite wave amplitudes both inside and outside the plasmasphere [Lee and Kim, 1999]. Observational studies have confirmed the existence of PVR, and they have frequencies in the Pi2 range [Takahashi *et al.*, 2009; Nosé, 2010; Luo *et al.*, 2011; Teramoto *et al.*, 2011; Ghamry *et al.*, 2015; Shi *et al.*, 2017]; they may also be classified as Pc4 waves [e.g., Takahashi *et al.*, 2005].

Multiple factors affect inner magnetosphere Pi2 wave frequencies, particularly during geomagnetically active conditions. During the course of a substorm, sources for Pi2 wave frequencies may include Bursty Bulk Flows [BBFs Kepko *et al.*, 2001], PVR [Lee and

70 *Kim, 1999*], Alfvén waves standing along the magnetic field, plasmopause surface waves,
71 and other mechanisms [*Keiling and Takahashi, 2011*]. Each mechanism has a unique fre-
72 quency dependence on plasma mass density, ionospheric conductivity, and other factors
73 that can change with time during the substorm. Thus, one may not expect observed Pi2
74 wave frequencies to remain stable before, during, and after a substorm or during other ge-
75 omagnetically active periods.

76 For example, the plasmasphere is generally expected to erode during substorms and
77 periods with southward Interplanetary Magnetic Field (IMF). Though erosion may not oc-
78 cur on timescales comparable to Pi2 event timescales, substantial erosion may well occur
79 between Pi2 events altering the Pi2 wave frequency from one event to the next. At the
80 same time ionospheric parameters such as density and conductivity may change rapidly
81 associated with the development of Sub-Auroral Polarization Streams (SAPS) [*Anderson*
82 *et al., 1993*]. SAPS are large, westward ionospheric flows observed during geomagneti-
83 cally active periods with peak flow speeds equatorward of the electron plasma sheet (en-
84 ergies on the order of one keV) precipitation boundary [*Foster and Vo, 2002*]. Ionospheric
85 density and conductivity variations due to SAPS and other phenomena may also affect the
86 properties of Pi2 waves [e.g., *Ream et al., 2015*].

87 The interpretation of observations in the context of one or more Pi2 wave models is
88 complicated by uncertainty about whether changing wave properties are due to changing
89 external conditions, density profiles, or a combination of the two. This study addresses
90 this complication by examining a two hour period with stationary plasmopause and vari-
91 able geomagnetic activity. This is made possible by a favorable satellite conjunction: (1)
92 multiple plasmopause crossings in the pre-midnight sector made by probes on similar or-
93 bits, (2) multiple plasmopause crossings in the pre-dawn sector made by probes on sim-
94 ilar orbits, (3) crossings overlap the region of wave activity and substorm/SAPS activity,
95 both spatially and temporally. As we shall show, a discrete frequency PVR is excited mul-
96 tiple times with a stable frequency before, during, and after a substorm. The substorm
97 and other geomagnetic activity have no effect on the PVR frequency due to the stationary
98 plasmopause, though they affect the spatial and temporal variation of wave amplitude.

99 **2 Instrumentation and Signal Processing**

100 In situ measurements of ULF waves and electron density are obtained from the Van
101 Allen Probes mission (also referred to as Radiation Belt Storm Probes, or RBSP). RBSP
102 is a two satellite constellation designed to study many aspects of radiation belt dynam-
103 ics [*Mauk et al., 2012*]. These probes have low inclination, elliptical orbits with geocen-
104 tric apogee near $5.8 R_E$ and nominal spin periods of roughly 11 seconds. The spin axis
105 nominally points towards the Sun. We use the Electric and Magnetic Field Instrument
106 Suite and Integrated Science [EMFISIS, *Kletzing et al., 2013*] high frequency plasma wave
107 measurement (measurements of a single electric field component from 10 to 500 kHz)
108 to determine the upper hybrid frequency and infer the electron density using the tech-
109 nique discussed by *Kurth et al. [2015]*. For ULF wave measurements, we examine spinfit
110 electric fields using the RBSP Electric Field and Waves instrument [EFW, *Wygant et al.,*
111 *2013*] spin plane booms. For the intervals examined in this study, the angle between the
112 spin axis and the background magnetic field is typically larger than 80 degrees, so it is
113 not generally possible to obtain the spin axis component of the electric field using the
114 $\vec{E} \cdot \vec{B} = 0$ approximation. We examined the electric field measured directly by the spin
115 axis boom, but it is affected by contamination in the DC and ULF frequency ranges due to
116 its short length/proximity to spacecraft. Additionally, the DC/ULF electric field from the
117 spin-axis boom measurement and $\vec{E} \cdot \vec{B} = 0$ do not agree during the period of interest.
118 Thus, we shall focus solely on the two spin plane measurements.

119 In addition to RBSP, we use Geostationary Operational Environmental Satellites
120 (GOES) and Time History of Events and Macroscale Interactions during Substorms (THEMIS)

129 **Table 1.** Ground magnetometer locations in geographic and corrected geomagnetic (CGM) coordinates.
 130 PGEO, UKIA, and CCNV are from the THEMIS array. FTN and FSJ are from the STEP array. VIC is from
 131 the CANMON array. FRN, BSL and FRD are from the USGS array. FSIM is from the CARISMA array.
 132 Geographic coordinates were obtained from the respective array websites or instrument papers, while CGM
 133 coordinates were obtained using the NASA Virtual Ionosphere, Thermosphere, Mesosphere Observatory
 134 via the online OMNIWeb interface by specifying each station’s geographic position, the 2010 version of the
 135 IGRF model modified slightly with predictive terms appropriate for 2013, and an altitude of 0 km. These
 136 coordinates may differ slightly from those reported elsewhere when using a different version of IGRF. Figure
 137 3 shows the map of geographic locations.

Station	Name	Geo Lat	Geo Lon	CGM Lat	CGM Lon
PGEO	Prince George	53.82	237.2	59.04	297.0
UKIA	Ukiah	45.14	241.1	51.15	304.0
CCNV	Carson City	39.19	240.2	44.99	304.5
FTN	Fort Nelson	58.90	237.2	64.09	295.1
FSJ	Fort Saint John	56.20	239.1	61.80	298.4
VIC	Victoria	48.52	236.6	53.61	298.0
FRN	Fresno	37.09	240.3	42.89	305.1
BSL	Stennis	30.35	270.4	40.73	342.1
FRD	Fredericksburg	38.20	282.6	48.04	359.4
FSIM	Fort Simpson	61.76	238.8	67.18	295.6

121 satellites for in situ measurements of ULF waves, particle injections, and densities at larger
 122 L shell. In particular, we use GOES satellite fluxgate magnetometers [*Singer et al.*, 1996]
 123 and electron detectors [*Onsager et al.*, 1996], specifically the magnetospheric electron de-
 124 tector (MAGED) telescope mounted at 0 degrees from the anti-Earthward direction [*Ro-*
 125 *driguez*, 2014; *Redmon et al.*, 2015], though other MAGED detectors yield qualitatively
 126 similar results for the purpose of this study. We also use observations of spacecraft poten-
 127 tial from the THEMIS satellites, which can be used to infer electron density [*McFadden*
 128 *et al.*, 2008; *Sibeck and Angelopoulos*, 2008].

138 For ground-based wave observations, we use magnetometer data from the THEMIS
 139 ground-based network [*Russell et al.*, 2008], Canadian Array for Realtime InvestigationS
 140 of Magnetic Activity (CARISMA) [*Mann et al.*, 2008], Canadian Magnetic Observatory
 141 Network (CANMON), Solar-Terrestrial Energy Program (STEP) polar network, and United
 142 States Geological Survey (USGS) [*Love and Finn*, 2011]. Table 1 shows the magnetic and
 143 geographic coordinates of each station. Data links with additional information about these
 144 stations are provided in the Acknowledgements.

145 For additional context on overall geomagnetic activity, ionospheric plasma flows,
 146 and wave activity, we use geomagnetic activity indices and propagated solar wind obser-
 147 vations, all-sky imagers, and mid-latitude high-frequency radars in the Super Dual Auroral
 148 Radar Network (SuperDARN). Geomagnetic activity indices and solar wind observations
 149 (propagated to the Earth’s bow shock) are obtained from the NASA Space Physics Data
 150 Facility OMNIWeb interface at <http://omniweb.gsfc.nasa.gov>. All sky imager (ASI) ob-
 151 servations are taken from the Fort Simpson (FSIM), Fort Smith (FSMI), Gillam (GILL),
 152 Fort Yukon (FYKN), and Sanikiluaq (SNKQ) stations in the THEMIS array via the pub-
 153 lic THEMIS database [*Mende et al.*, 2008]. SuperDARN measurements are taken from
 154 a public database at Virginia Tech. These radars measure the line-of-sight (LOS) veloc-

ity component of the ionospheric plasma drift in the F-region. Multiple radars can be used together to derive global maps of the electric potential and flow patterns in the ionosphere using standard tools available on the Virginia Tech website [Ruohoniemi and Baker, 1998]. Most radars operate in a mode that sweeps the radar field of view every 1-2 minutes. However, special modes are available at higher resolution. In this study, we show measurements from the Fort Hays West (FWH) and Christmas Valley East (CVE) radars when operating in the RBSP mode, with select beams sampling at 19s cadence.

For wave analysis in the frequency domain, we examine dynamic power spectra of the magnetic and electric field, where all signals are first interpolated to have the same 11s time resolution (the lowest resolution across all measurements that were analyzed in the frequency domain) using the nearest neighbor technique. Throughout the manuscript, dynamic power spectra are obtained using a running 128 point (23.5 minute) Discrete Fourier Transform (DFT) with 94% window overlap. Prior to taking the DFT, a line is fit to the data in the 23.5 minute window and subtracted from the original data to obtain perturbation fields, and a Hanning window is applied to reduce spectral leakage. The power spectrum is then computed using a three point smooth over frequency to improve the signal to noise ratio of the coherent ULF pulsation over the incoherent background noise. In Figures 6 and 9 we also examine normalized dynamic power spectra to focus on the time evolution of spectral features; these are obtained by dividing the power in each frequency bin by the maximum power in the 5-20 mHz frequency band at each time step. Finally, in the bottom panel of Figure 6 and bottom right of Figure 7, we high-pass filter time series using a 5 mHz cutoff to more easily examine amplitude and phase differences between signals.

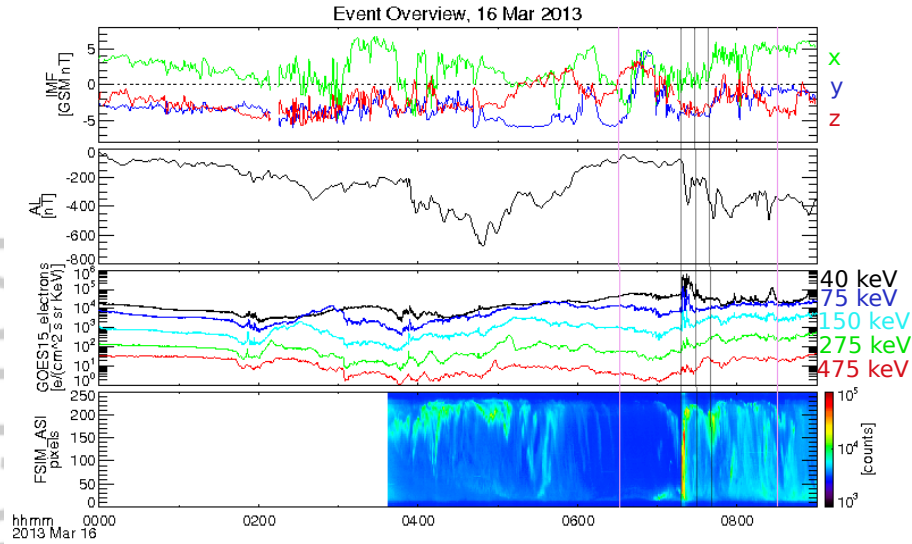
The DFT frequency bin width is 2.13 mHz when using the 128 point window and 3-point smoothing. Thus, when we identify frequencies based on a power spectrum peak, there is an uncertainty of roughly ± 1.1 mHz. To better assess the wave frequency stability, we use a longer 256 point DFT window with 3-point smoothing in panel 8 of Figure 6, increasing the frequency resolution by a factor of two at the expense of capturing some temporal variations. Generally, when we refer to a discrete frequency of 8 mHz in this study, it should be understood there is some uncertainty in the frequency determination, either ± 1.1 mHz or ± 0.53 mHz depending on the DFT window length, and that the peak frequency may vary slightly depending on the choice of DFT window length and amount of smoothing in frequency domain. For example, the frequency bin with peak PVR power is 7.8 mHz when using the 128 point window with 3-point smooth, while it is 8.2 mHz when using the 256 point window with 3-point smooth. To avoid confusion, we simply refer to this as an 8 mHz signal throughout. The only exception occurs when discussing the stability of the PVR frequency; in that discussion, we shall directly reference this uncertainty as 8.2 mHz ± 0.53 mHz, based on the lower and upper bounds of the frequency bin corresponding to the power spectrum peak observed by low latitude ground magnetometers, when using the 256 point DFT window.

Finally, we note that when comparing dynamic power spectra constructed using the interpolated 11s ground magnetometer time series and the original 1s time series, there were no significant differences in the frequency band of interest, 5-20 mHz. This suggests that 11s samples (Nyquist frequency 45 mHz) are sufficient to capture the wave activity of interest.

3 Observations

3.1 Solar wind and geomagnetic activity overview

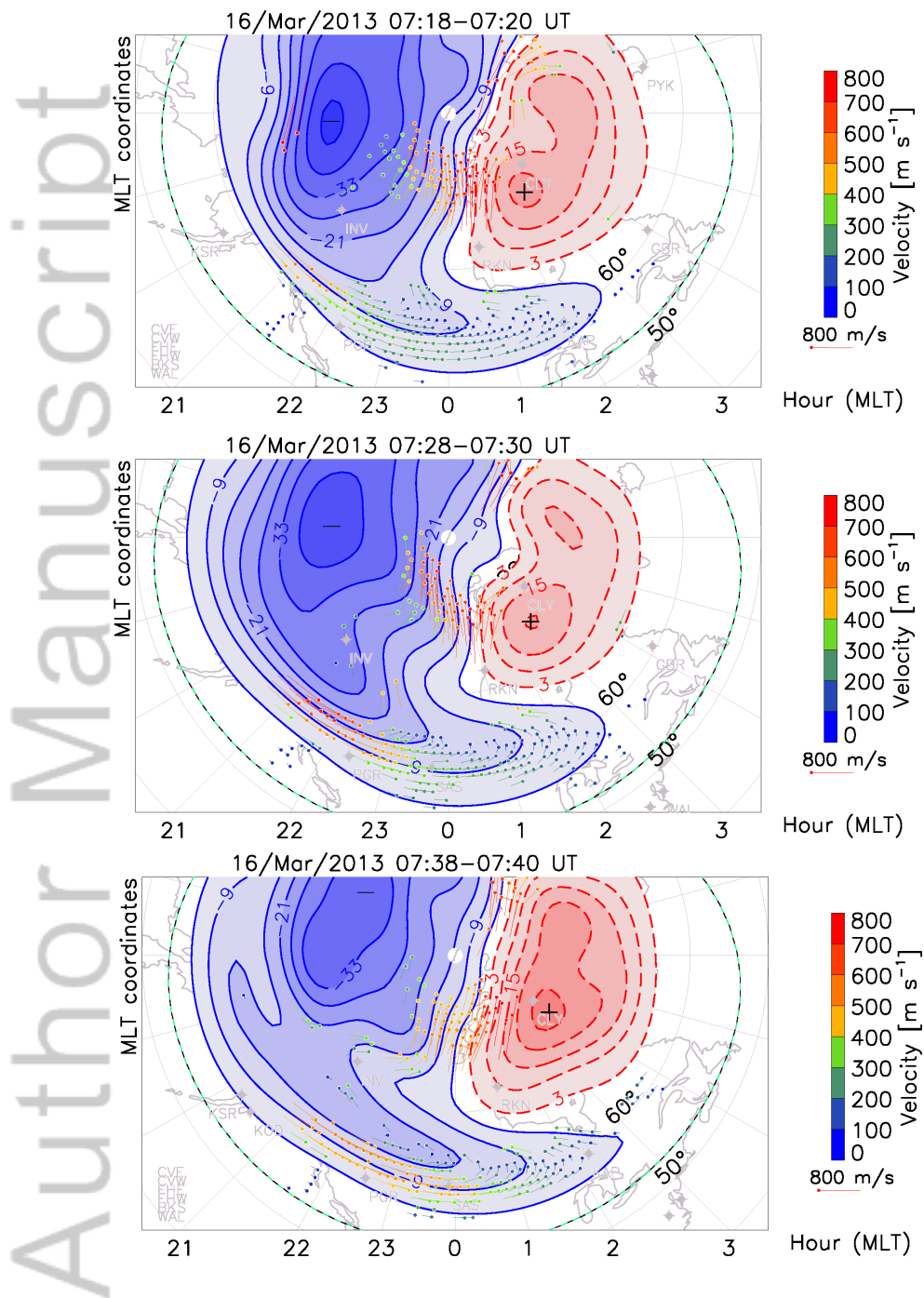
The ULF wave event occurred on 16 March 2013, with the period of interest 0630-0830 UT. Figure 1 shows an overview of the interplanetary magnetic field (IMF) and geomagnetic activity during 0000-0900 UT, with the interval of interest for Pi2 wave activ-



202 **Figure 1.** Top: From top to bottom, (1) OMNIWeb Interplanetary Magnetic Field in GSM coordinates
 203 and propagated from measurement location to the Earth's bow shock, (2) AL index, (3) electron energy flux
 204 measurements from GOES-15 MAGED detector oriented at 0 degrees from the anti-Earthward direction with
 205 different energy channels center energies indicated by color, (4) Fort Simpson (FSIM) all sky imager keogram
 206 showing intensity in color. Two pink lines indicate the interval of interest for Pi2 wave activity, while three
 207 gray lines indicate times corresponding to flow patterns shown in Figure 2.

214 ity marked by pink lines. The top panel shows the time shifted (to bow shock nose) IMF
 215 measurement in GSM coordinates from OMNIWeb. The IMF is southward for much of
 216 the day, but it turns northward at 0630 UT. A southward turning of the IMF occurs be-
 217 tween 0700 and 0710 UT, after which the z component remains negative for roughly the
 218 next 40 minutes. During this period, the solar wind flow speed and dynamic pressure (not
 219 shown) are mostly steady at roughly 450 km/s and 1.7 nPa, respectively. There are some
 220 small variations in speed and pressure prior to 0700 UT, though these do not appear to
 221 have a direct impact on Pi2 wave properties in the magnetosphere thus will not be dis-
 222 cussed further.

223 The second panel in Figure 1 is for the AL index obtained from OMNIWeb. For
 224 much of the early part of the day, AL is below -200 nT with several sharp decreases to
 225 lower values, such as the period just before 0400 UT. At the beginning of the 0630-0830
 226 UT period of interest, AL is closer to 0 indicating quiet conditions. A rapid decrease in
 227 AL at 0720 UT is associated with substorm activity, with substorm onset at 0716 UT
 228 within the THEMIS FSIM ASI field-of-view (fourth panel). This is consistent with ener-
 229 getic electron measurements from the GOES-15 satellite. In particular, differential electron
 230 fluxes from the GOES-15 MAGED detector oriented at 0 degrees from the anti-Earthward
 231 direction are shown in the third panel of Figure 1, with energy labels corresponding to
 232 the center energies of different channels. These data indicate that GOES-15, located at
 233 geostationary orbit near 22 MLT, observes an electron injection at the onset time; note
 234 that the other GOES-15 MAGED telescopes as well as GOES-15 proton detectors observe
 235 the same injection timing and qualitatively similar results for the purpose of this study
 236 (not shown). Finally, the rapid decrease in AL is also consistent with the keogram gener-
 237 ated using measurements from the FSIM ASI in the fourth panel of Figure 1; FSIM is at
 238 a similar MLT as the GOES spacecraft, and it observes the westward traveling surge about



208 **Figure 2.** Global maps of the ionospheric electric potential and flow pattern derived from fits to measure-
 209 ments from multiple SuperDARN radars at 0720 UT, 0730 UT, and 0740 UT (times indicated by gray lines in
 210 Figure 1).

239 one minute after the initial onset at FSIM (see panel 2 of Figure 6 for more detail with
240 shorter time range).

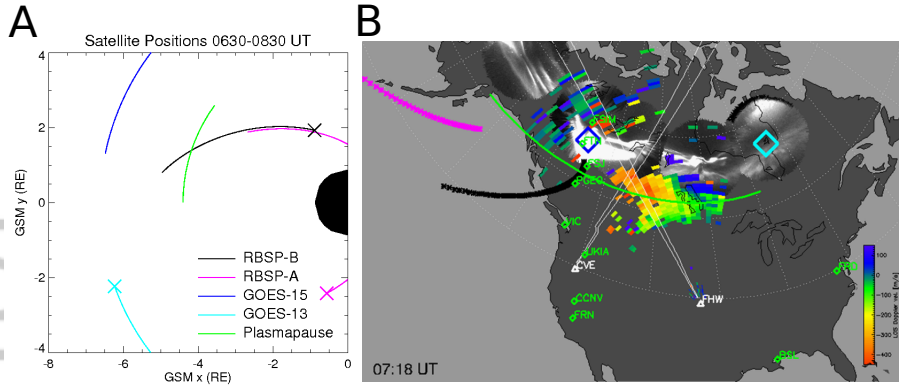
241 Figure 2 shows ionospheric flows associated with the substorm activity at 0720,
242 0730, and 0740 U (times indicated in Figure 1 by gray lines). Flow directions are indi-
243 cated by dots and lines where the base of the vector is the dot, and velocity magnitude
244 is indicated by both color and the length of the line. These figures were generated by a
245 spherical harmonic regression mapping procedure using LOS velocity measurements from
246 all the SuperDARN radars in the northern hemisphere [Ruohoniemi and Baker, 1998]. A
247 large, westward directed flow develops at 0720 UT near 21-22 MLT, as indicated by the
248 flow pattern on the top. It intensifies by 0730, with flows reaching 800 km/s, as indicated
249 by the middle flow pattern figure. The region with the large westward flow also spreads
250 eastward. Finally, the flow pattern at 0740 UT (bottom) indicates that the region with
251 large flows continues to spread eastward, but the flows begin to weaken.

252 In summary, Figure 1 indicates southward IMF and several sharp decreases in AL
253 for much of the early part of the day, then relatively quiet conditions in the nightside mag-
254 netosphere at the beginning of the interval of interest, 0630 UT, until roughly 0716 UT
255 when a substorm occurs. Following this, a region of large, westward flow intensifies and
256 spreads in the mid-latitude ionosphere, as shown in Figure 2. These observations are con-
257 sistent with the definition of SAPS [Foster and Vo, 2002] and the SAPS evolution after
258 substorm onset [Zou *et al.*, 2009a,b, 2012]. Zou *et al.* [2009a,b] showed that SAPS in-
259 creased equatorward of the auroral onset as a consequence of field-aligned current clo-
260 sure. In this case, auroral onset is initiated close to FSIM, with SAPS initially developing
261 equatorward of FSIM and spreading eastward at later times.

262 3.2 Plasmapause Location

263 In this section we identify the location of the plasmapause in electron density data
264 and show where in situ and ground-based observations are located relative to the plasma-
265 pause. Figure 3A is for the satellite orbits in the GSM xy plane from 06:30-08:30 UT.
266 Figure 3B is for the ground station positions (green diamonds) and locations of Super-
267 DARN beams that will be analyzed in a later figure (white lines). Using the IGRF model
268 combined with the Tsyganenko [1989] external magnetic field model (results are similar
269 when using other external models), we map nightside satellite locations from the magne-
270 tosphere to the ground: RBSP-A (pink crosses), RBSP-B (black crosses), GOES-13 (light
271 blue diamond), and GOES-15 (dark blue diamond). For global context a solid green line
272 indicates the plasmapause location at $L \sim 4.4R_E$, determined using analysis in the next
273 Figure. Additional context is provided by all sky images taken from FYKN, FSIM, FSMI,
274 GILL, and SNKQ at 0718 UT, i.e., roughly two minutes after the substorm onset; these
275 show the location of a large auroral arc associated with the substorm mentioned in the
276 previous section (note that mid-latitude stations in North America were affected by cloud
277 cover during this event). Finally, LOS velocities measured using the FHW SuperDARN
278 radar are shown in color, also from 0718 UT. Larger flows are generally seen adjacent and
279 just poleward of the plasmapause footprint, consistent with the SAPS flows observed in
280 the SuperDARN data. Note that the most westward beams are more closely aligned with
281 the SAPS flow direction, and that color variations are due to both spatially varying flows
282 and spatially varying beam directions.

301 Figure 4 shows electron density measurements from five different satellites during
302 periods when each satellite was closest to the plasmapause. From top to bottom, Figure
303 4A shows electron density time series for RBSP-B, RBSP-A, THEMIS-D, THEMIS-E,
304 and THEMIS-A. Figure 4B shows the satellite trajectories during the periods when these
305 measurements were taken: RBSP-B from 0630-0845 UT (solid black line), RBSP-A from
306 0745-1030 UT (solid pink line), THEMIS-D from 0400-0600 UT (dashed black line),
307 THEMIS-E from 0630-0830 UT (dashed blue line) and THEMIS-A from 1115-1315 UT



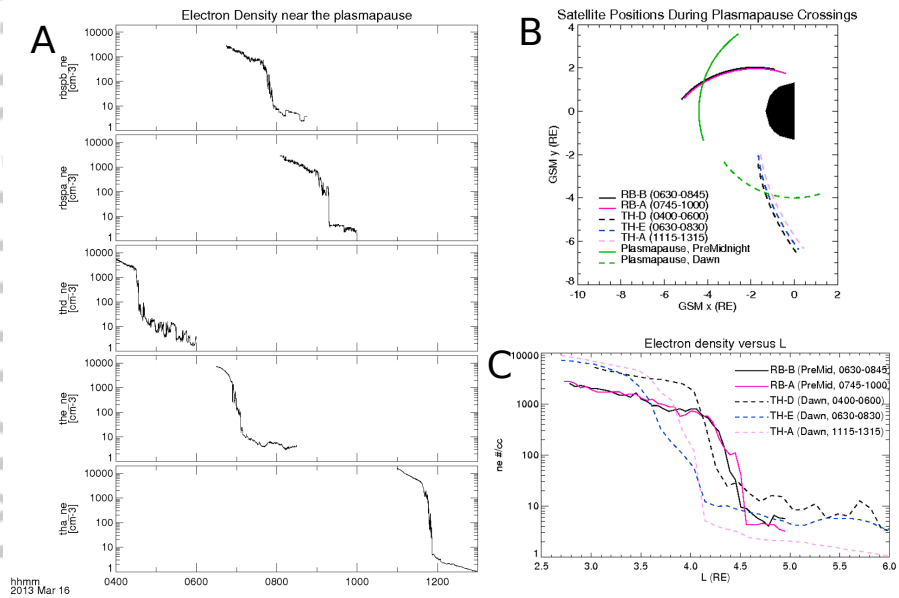
283 **Figure 3.** A: GSM xy view of satellite trajectories from 0630-0830 UT. Lines with different color indi-
 284 cate different satellites and the plasmopause location (green line) determined from RBSP electron density
 285 measurements. Crosses mark the start of the spacecraft trajectories at 0630 UT. B: Map showing the ge-
 286 ographic position of ground magnetometer stations as green diamonds and the Fort Hays West/Christmas
 287 Valley East SuperDARN radars as white triangles, the ground track of RBSP-B (black crosses), RBSP-A (pink
 288 crosses), GOES-15 (dark blue diamond) and GOES-13 (light blue diamond) from 0630-0830 UT, with col-
 289 ors consistent with panel A. Two SuperDARN beams selected for analysis are marked with white lines. The
 290 plasmopause location derived from RBSP measurements is shown as a green line. Snapshots at 0718 UT of
 291 the FYKN, FSIM, FSMI, GILL, and SNKQ all sky camera images (whiter color indicates stronger intensity)
 292 and Fort Hays West radar line of sight velocities (color scale at right) are overlotted on the map.

308 (dashed pink line). Both RBSP spacecraft are in the pre-midnight sector on similar orbits,
 309 while the three THEMIS spacecraft are near the dawn sector on similar orbits.

310 Figure 4C shows electron density measurements binned according to dipole L from
 311 the five spacecraft, with line styles consistent with panel B; measurements from the pre-
 312 midnight sector are solid lines while dawn sector measurements are dashed lines. We
 313 identify the plasmopause location as the location of sharpest density gradient. The radial
 314 density profile evolves little in the pre-midnight sector between the RBSP-B (0630-0845
 315 UT) and RBSP-A (0745-1030 UT) outbound passes, as indicated by the solid black and
 316 pink lines lying nearly on top of each other. Moreover, the plasmopause location does not
 317 change between subsequent crossings at 0750 UT (RBSP-B) and 0920 UT (RBSP-A). In
 318 the dawn sector, the plasmopause moves inward from the location where THEMIS-D first
 319 measures it at 0430 UT (dashed black line) to the location where THEMIS-E observes
 320 it at 0655 UT (dashed light blue line). At 1145 UT, THEMIS-A observes it in the same
 321 location (dashed pink line), suggesting that the plasmopause remained stationary for ~5
 322 hours.

323 Note that THEMIS densities are inferred from spacecraft potential, and the techni-
 324 que to obtain the density is significantly less accurate in high-density regions [Kwon
 325 *et al.*, 2015] depending on several factors [Laakso and Pedersen, 1998]. Thus, though the
 326 plasmopause identification using THEMIS satellites is reliable, the absolute accuracy of
 327 densities at low L is not particularly reliable and we do not stress comparisons between
 328 satellites at low L values.

329 We estimate the plasmopause location (sharpest gradient) to be at $L \sim 4.4$ in the pre-
 330 midnight sector and $L \sim 4.0$ in the pre-dawn sector during the period of interest. Figure 4B
 331 shows the plasmopause location in the pre-midnight sector inferred from the RBSP ob-



293 **Figure 4.** A) Electron density measurements from five different satellite trajectories (from top to bottom):
 294 RBSP-B from 0630-0845 UT, RBSP-A from 0745-1030 UT, THEMIS-D from 0400-0600 UT, THEMIS-E
 295 from 0630-0830 UT and THEMIS-A from 1115-1315 UT. B) Orbital trajectories for each spacecraft cor-
 296 responding to times shown in panel A: RBSP-B (solid black line), RBSP-A (solid pink line), THEMIS-D
 297 (dashed black line), THEMIS-E (dashed blue line) and THEMIS-A (dashed pink line). The approximate
 298 plasmopause location from RBSP observations in the pre-midnight sector is shown as a solid green line, while
 299 the location based on THEMIS observations near dawn is shown as a dashed green line. C) Electron density
 300 versus L using the same data as in panel A and the same linestyles as in panel B.

332 observations as a solid green line, while the dawn sector plasmopause from THEMIS-A and
333 THEMIS-E is a dashed green line. Figure 3A and 3B also show the plasmopause location
334 in the pre-midnight sector as a solid green line. These figures show that the two GOES
335 spacecraft are located outside the plasmasphere and GOES-15 maps near the region of the
336 auroral intensification at 0722 UT. In contrast, the two RBSP spacecraft are mostly inside
337 the plasmasphere until the end of the interval, when RBSP-B crosses outside the plasmas-
338 phere.

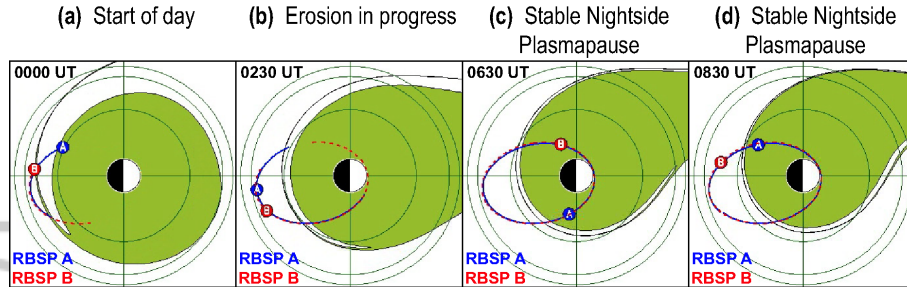
339 There are many factors that control the plasmopause location in a given local time
340 sector, including the current and previous convection electric field, refilling rates, and the
341 previous history of the plasmasphere in other local time sectors. The observations sug-
342 gest that in this particular event, the balance between all of these factors led to a stable
343 plasmopause location between 0630-0830 UT. There are several lines of evidence from
344 Figures 1 and 4 to support this claim:

- 345 1. Multiple THEMIS satellite passes demonstrate the plasmopause location evolved
346 between 0430 and 0655 UT in the pre-dawn sector, but it did not change substan-
347 tially between 0655 UT and 1145 UT. If the primary cause of erosion and plasma-
348 pause motion is changes to the global convection electric field caused by southward
349 IMF, one would expect changes to plasmopause location to be global in nature; if
350 the plasmopause is stationary near dawn, it will be stationary near midnight.
- 351 2. Multiple RBSP satellite passes are consistent with (1), indicating no significant
352 change in plasmopause location in the pre-midnight sector between 0750 UT and
353 0920 UT. The only difference between the plasmopause locations near midnight and
354 dawn is due to the expected inward motion of cold plasma as it $\vec{E} \times \vec{B}$ drifts east-
355 ward.
- 356 3. Plasmopause motion observed by THEMIS satellites between 0430 UT and 0655
357 UT likely concluded before 0630 UT. Before 0600 UT, geomagnetic activity levels
358 were decreasing and the north-south component of the IMF was close to 0 (Figure
359 1). Since the typical timescale for the plasmopause to move in response to IMF
360 variations is 10-30 minutes [Murakami *et al.*, 2007], plasmopause motion should
361 have concluded by 0630 UT.
- 362 4. There is no indication of local plasmopause structures [Goldstein *et al.*, 2005] in
363 either the THEMIS or RBSP density profiles.

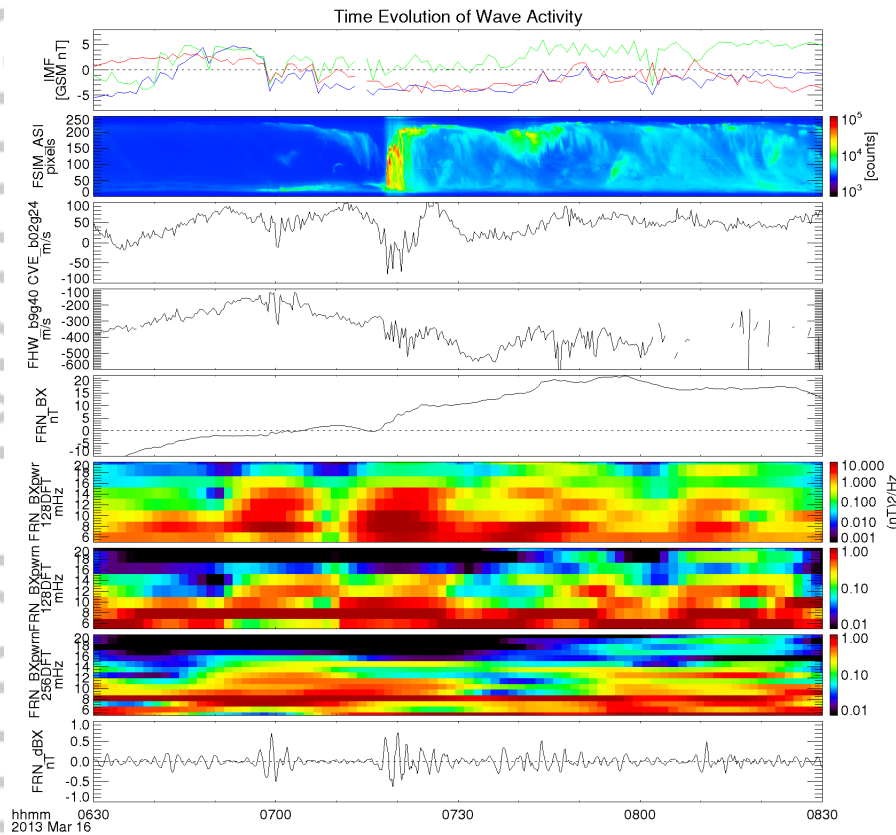
364 Thus, geomagnetic activity and periods of southward IMF during the 0630-0830 UT pe-
365 riod may have led to changes in the convection electric field, but these variations did not
366 cause significant plasmopause motion. For global context and as a final confirmation of
367 this scenario, we examined Plasmopause Test Particle (PTP) simulations that have been
368 shown to closely reproduce RBSP plasmopause observations [Goldstein *et al.*, 2014]. The
369 time varying plasmopause location is obtained using an ensemble of cold test particles that
370 $\vec{E} \times \vec{B}$ drift, where the convection electric field is obtained from solar wind measurements
371 and the Kp index. Figure 5 shows output of the simulation at four times before, during
372 and after the Pi2 wave analysis interval. Confirming the interpretation of the satellite mea-
373 surements, there is an erosion event during the first few hours of 16 Mar 2013 (panels a
374 and b), followed by relatively stable nightside plasmopause location during the wave analy-
375 sis period 0630-0830 UT (panels c and d).

380 3.3 Pi2 wave activity before, during, and after substorm

390 Having examined overall geomagnetic activity and plasmopause location, we next
391 examine the spatial and temporal evolution of wave properties. Figure 6 examines the time
392 evolution of wave activity and relationship to potential driving mechanisms. The top two
393 panels are identical to panels 1 and 4 of Figure 1 but for the shorter 0630-0830 UT period
394 of interest; they are provided for context on the times of different auroral activations and



376 **Figure 5.** Each panel shows the plasmasphere in green, based on output from the PTP simulations. The
 377 location and orbits of the RBSP-A (blue) and RBSP-B (red) satellites are also shown. Each panel is for a
 378 different time, with the last two panels (third and fourth from left) corresponding to the beginning and end of
 379 the Pi2 wave analysis interval.



381 **Figure 6.** From top to bottom: (1) OMNIWeb IMF in GSM coordinates (same as Figure 1), (2) keogram
 382 from Fort Simpson all sky imager (same as Figure 1), (3) line-of-sight velocity measured by the SuperDARN
 383 Christmas Valley East radar at beam 2 and gate 24, (4) the same for the Fort Hays West radar at beam 9 and
 384 gate 40 (note that these beams and gates correspond to the location where the two radar beams overlap in
 385 Figure 3), (5) north-south component of magnetic field, BX, measured by FRN ground station, (6) dynamic
 386 power spectrum for BX at FRN, (7) normalized BX power spectrum at FRN, where the power spectrum at
 387 each time step is normalized to the maximum power in the 5-20 mHz frequency band, (8) the same as 7,
 388 but using a DFT window that is twice as long (256 compared to 128 point, or 47.0 minutes compared to 23.5
 389 minutes), (9) high-pass filtered BX at FRN with 5 mHz cutoff.

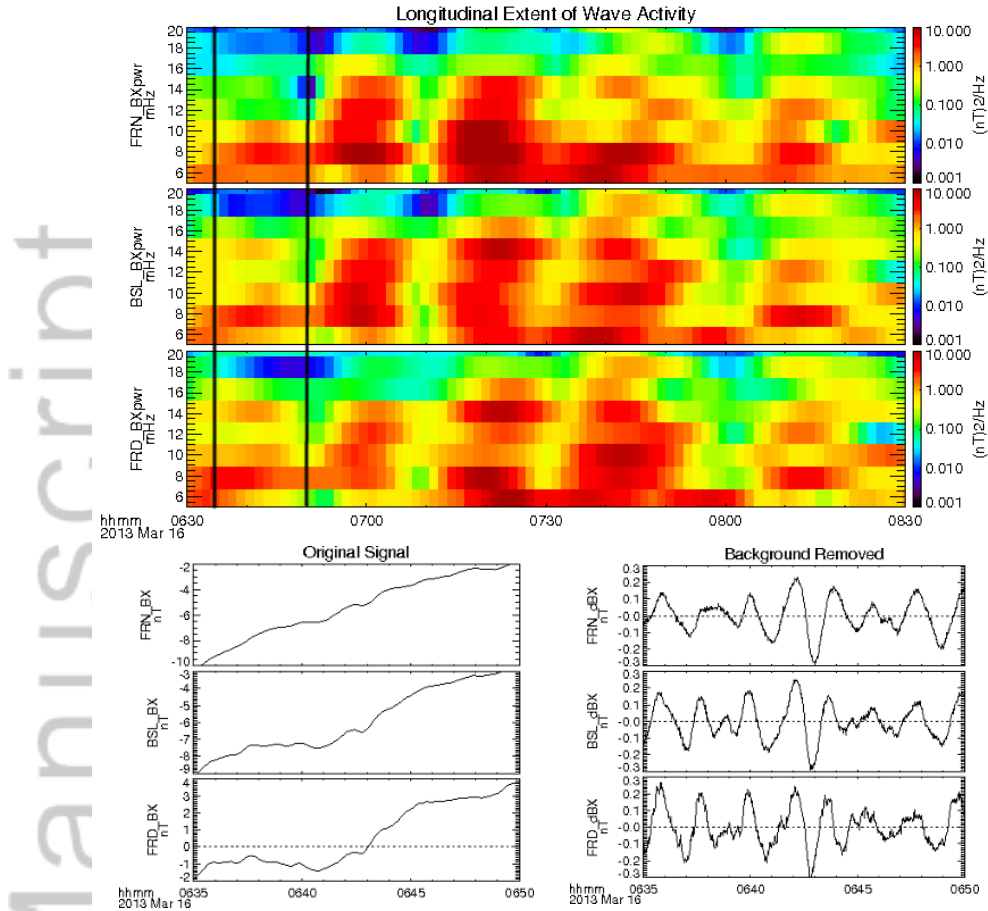
395 solar wind driving conditions. The third and fourth panels are for line-of-sight velocities
396 measured by the SuperDARN Christmas Valley East (CVE) radar at beam 2 and range
397 gate 24 and Fort Hays West (FHW) radar at beam 9 and range gate 40. These beams and
398 range gates correspond to the location where the two radar beams overlap in Figure 3B,
399 in the region of intense SAPS flows. Note that while neither beam is exactly aligned with
400 the SAPS flow direction, the FHW beam is more closely aligned with the flows while the
401 CVE beam is nearly orthogonal to them (see Figures 2 and 3B). This is consistent with
402 the LOS flow measurements in panels 3 and 4 of Figure 6. While the CVE measurement
403 shows fairly stable 50 m/s flows throughout the interval (panel 3), the FHW beam shows a
404 rapidly changing background flow, starting at -100 m/s at 0700 UT and decreasing to -600
405 m/s by 0730 UT (panel 4). Since the FHW beam is most closely aligned with the SAPS
406 flow direction, this trend is indicative of the increasing SAPS flows.

407 ULF perturbations with frequencies in the Pi2 range are also seen throughout the
408 interval in both radars, though the signal is sometimes obscured by the time varying back-
409 ground SAPS flows. The fifth panel of Figure 6 is for the north-south magnetic field (BX)
410 measured by the FRN ground magnetometer station (daily average subtracted), while the
411 sixth panel is for the corresponding dynamic power spectrum; this station is located equa-
412 torward of the SuperDARN LOS flow measurement locations (see Figure 3B and Table 1
413 for location). As shown in the sixth panel, several intensifications in wave power are ob-
414 served at 8 mHz, in some cases accompanied by intensifications at other wave frequencies.
415 For example, during the auroral intensification at the beginning of the substorm at 0720
416 UT, wave power is largest at 8 mHz (dark red color) but the power spectrum has a broad
417 peak with wave power at other higher and lower frequencies (lighter red colors above and
418 below 8 mHz). To more clearly examine the time evolution of wave spectral features, the
419 power spectrum at each time step is normalized to the maximum power in the 5-20 mHz
420 frequency band in the seventh panel of Figure 6. As evidenced by the dark red band ex-
421 tending across nearly the entire figure, the dominant spectral feature occurs at 8 mHz. In
422 other words, there is a peak in the power spectrum at 8 mHz for the majority of the two
423 hour interval. However, we note that there are several intervals where the peak frequency
424 is lower (e.g., red line at 6 mHz at 0800 UT). These correspond to periods where the 8
425 mHz signal weakens relative to other wave activity and may not be detectable (panel 6).
426 We return to this point in section 4.

427 To better resolve the frequency of these waves and assess the stability of the 8 mHz
428 signal during the period of interest, we doubled the DFT window length (256 point, 47
429 minutes) in panel 8 of Figure 6. Recall from section 2 that this increases the frequency
430 resolution by a factor of two. The results are similar to panel 7 with a more narrow red
431 line that extends across the Figure. Based on these results and the width of the DFT fre-
432 quency bins, we conclude that the dominant spectral feature observed at FRN occurs at
433 a frequency of 8.2 ± 0.53 mHz during most of the two hour interval. In a future study,
434 more sophisticated signal processing tools could be used to better resolve the frequency.
435 In the present study, we can at least say the frequency was stable in the range of $8.2 \pm$
436 0.53 mHz through multiple intensification during the two hour interval (note the 47 minute
437 DFT windows near the beginning of the two hour interval do not overlap with those at the
438 end).

439 Finally, the ninth panel shows high-pass filtered BX time series at FRN to more di-
440 rectly compare with SuperDARN LOS flow time series in panels 3 and 4. Intensifications
441 in 8 mHz wave activity occur at 0700 and 0720 UT in all three time series.

442 More information about the global extent of wave activity observed at low latitudes
443 is shown in Figure 7. The top three panels are for the BX dynamic power spectrum at the
444 FRN (same as panel 6 in Figure 6), BSL, and FRD stations, respectively. These stations
445 extend across roughly 55 degrees magnetic longitude (roughly 3.5 hours MLT) and 5 de-
446 grees magnetic latitude. Despite their spatial separation, they observe similar temporal
447 evolution of the wave power spectrum, though FRN tends to observe slightly larger wave



450 **Figure 7.** Top: From top to bottom, BX dynamic power spectrum at the FRN, BSL, and FRD ground mag-
 451 netometers. Solid lines mark the time interval analyzed in the bottom of the figure. Bottom Left: From top
 452 to bottom, the original (apart from daily average subtraction) north-south magnetic field measurement at the
 453 FRN, BSL, and FRD stations between 0635-0650 UT. Though small compared to background trends, there
 454 are noticeable perturbations with roughly 2 minute periodicity. Bottom right: The same as bottom left, but
 455 with background trends removed using a high-pass filter with 5 mHz cutoff. Though separated by several
 456 degrees in magnetic latitude and longitude, all three stations observe similar perturbations with very small
 457 time lags.

448 powers likely due to its proximity to the most intense auroral intensification (Figure 3B),
 449 consistent with previous studies of Pi2 waves [Nosé *et al.*, 2006].

458 The bottom of Figure 7 illustrates the similarities in wave activity at these three sta-
 459 tions by examining the relatively quiet 0635-0650 UT interval. The bottom left shows the
 460 original (apart from daily average subtraction) north-south magnetic field measurement at
 461 FRN, BSL, and FRD. Though the background trend is larger than the perturbation ampli-
 462 tudes, perturbations with similar periods can still be seen at all stations. The bottom right
 463 further illustrates the similarities in wave activity by showing the signal with background
 464 trend removed using a high-pass filter with 5 mHz cutoff. During this 15 minute
 465 interval, 8 mHz fluctuations with similar amplitude are seen at all stations with almost no time lag.
 466 Given the roughly 3.5 hour MLT and 5 degrees latitude separation of these stations, this
 467 similarity suggests the waves are globally coherent with negligible frequency change ver-
 468 sus latitude or longitude. Note that the perturbation amplitudes are roughly 10 times larger

469 than the sensitivities of the USGS magnetometers [0.01 to 0.02 nT, *Worthington et al.*,
470 2009].

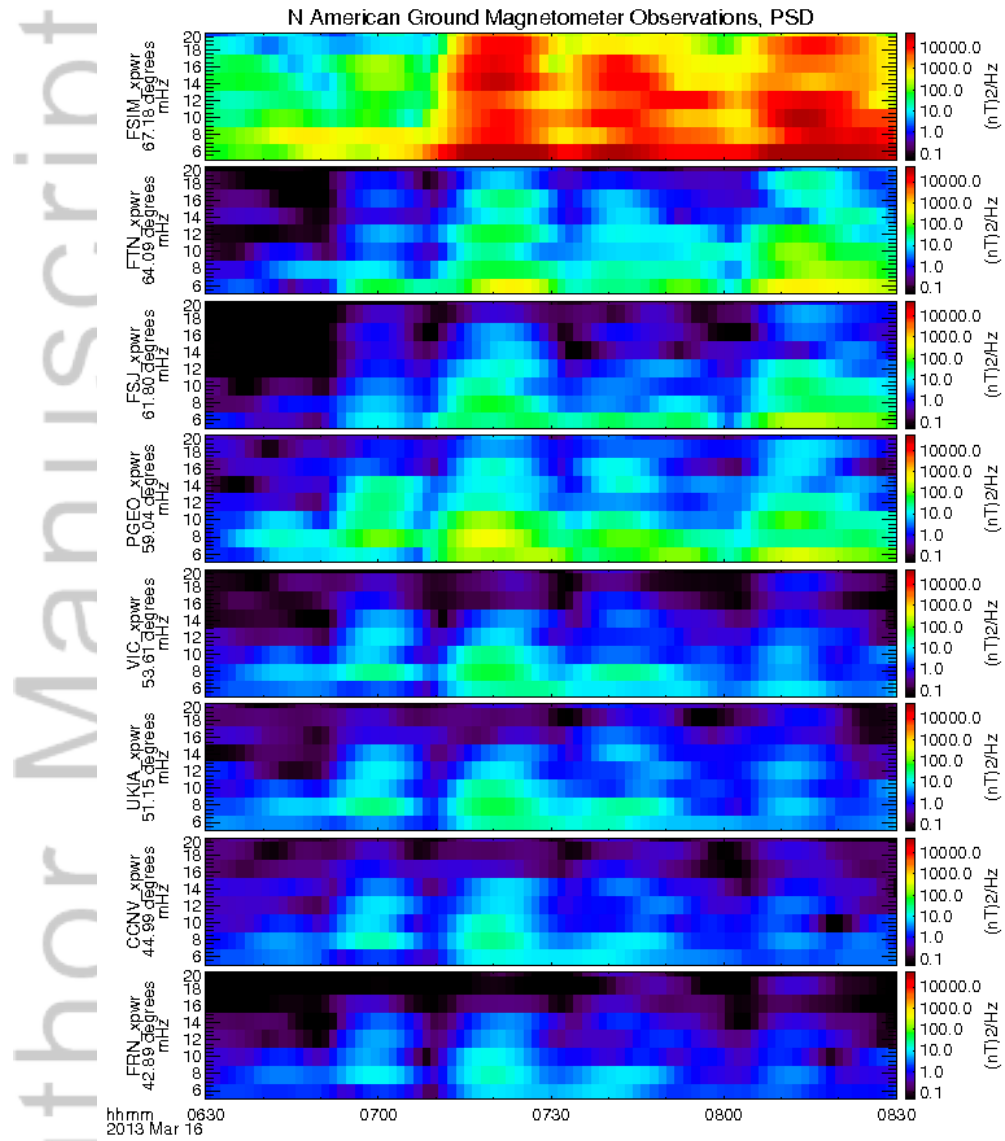
475 We next examine how wave properties vary with magnetic latitude. Figure 8 shows
476 dynamic power spectra from ground magnetometer stations along a similar meridian in
477 western Canada and the United States (Figure 3B). Stations are ordered from highest lati-
478 tude on top to lowest latitude at the bottom: FSIM, FTN, FSJ, PGEO, VIC, UKIA, CCNV,
479 FRN. Recall from Figure 3B that PGEO and FSJ are closest to the plasmopause and that
480 FSJ, FTN, and FSIM all map to locations outside the plasmopause. All dynamic power
481 spectra are plotted using the same scale. The lowest latitude FRN, CCNV, UKIA, and
482 VIC stations tend to observe the smallest wave amplitudes (blue-green colors at most
483 frequencies/times), PGEO, FSJ, and FTN observe intermediate amplitudes (green colors
484 at most frequencies and times), while FSIM observes significantly larger wave ampli-
485 tudes (yellow and red colors at most frequencies/times). The 8 mHz signal seen in ear-
486 lier figures appears most clearly at the lower latitude stations, though all stations observe
487 it during periods when other wave activity with more broadband frequency spectra is not
488 present, such as the 0635-0650 UT interval.

489 Figure 9 is the same as Figure 8, except the power spectra have been normalized
490 in the same manner as in Figure 6, panel 7. The 8 mHz signal dominates the normalized
491 spectra throughout the two hour interval for stations at latitudes below 60 degrees, as in-
492 dicated by the solid red band across the bottom five panels at 8 mHz. At higher latitudes,
493 the 8 mHz signal is also present for at least part of the interval, but as discussed above it
494 is less often the dominant spectral feature. For example, there are intervals where the peak
495 frequency is lower (i.e., red line at 6 mHz for most of the interval in the top three panels).
496 The disappearance of the red band at 8 mHz does not necessarily indicate that the original
497 8 mHz wave activity has damped out. Instead, these monochromatic waves may be ob-
498 scured by larger amplitude wave activity with a more broadband frequency spectrum that
499 overlaps 8 mHz. We return to this point in section 4.

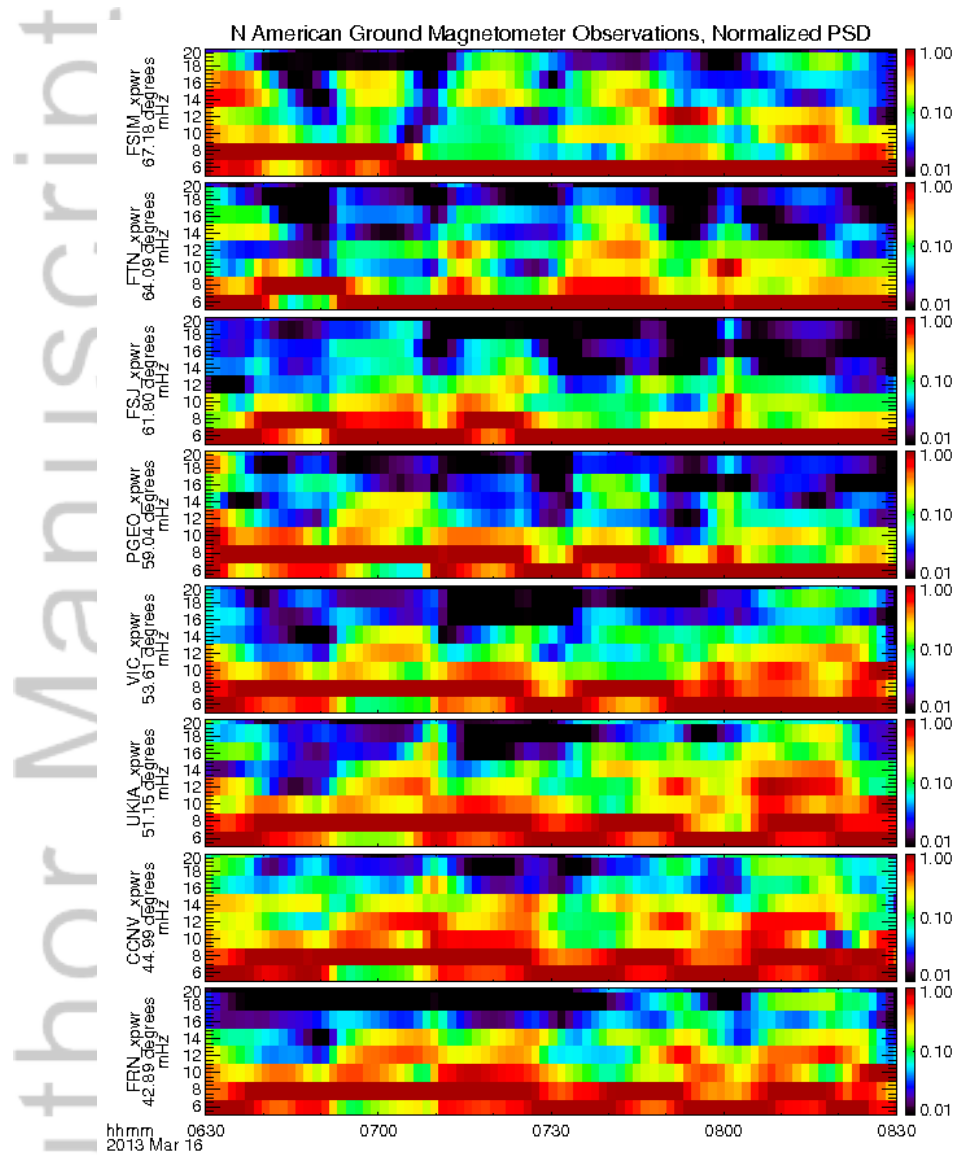
503 We next turn our attention to in situ GOES-15 and GOES-13 satellite measurements
504 of wave activity outside the plasmopause. The first and fourth panels of Figure 10 are for
505 the three components of the magnetic field in GSM coordinates measured by GOES-15
506 and GOES-13, respectively. When compared to GOES-13, the GOES-15 magnetic field
507 experiences a much larger deflection near 0718 UT, accompanied by larger fluctuations.
508 This is roughly the time the particle injection was observed by GOES-15 (Figure 1) and
509 when the large auroral arc was observed near the footpoint of GOES-15 (fourth panel of
510 Figure 1 and Figure 3B). These observations indicate the largest disturbances associated
511 with the substorm are in the pre-midnight sector near the GOES-15 satellite location. This
512 is also reflected in the second and fifth panels, showing total magnetic field measured by
513 GOES-15 and GOES-13, respectively. Noting the y-axis scale difference, GOES-15 ob-
514 serves generally larger total magnetic field perturbations than GOES-13.

518 The third and sixth panels of Figure 10 are for the dynamic power spectrum of the
519 total magnetic field observed by GOES-15 and GOES-13, respectively. GOES-15 ob-
520 serves systematically larger amplitude fluctuations at most frequencies and times. Given
521 the spacecraft positions (Figure 3A), this suggests wave activity outside the plasmasphere
522 is more intense pre-midnight when compared to post-midnight. Generally, compressional
523 wave activity observed by both GOES probes has a broader frequency spectrum than wave
524 activity observed on the ground, with the frequency range of enhanced wave power includ-
525 ing, but not necessarily peaking at, 8 mHz.

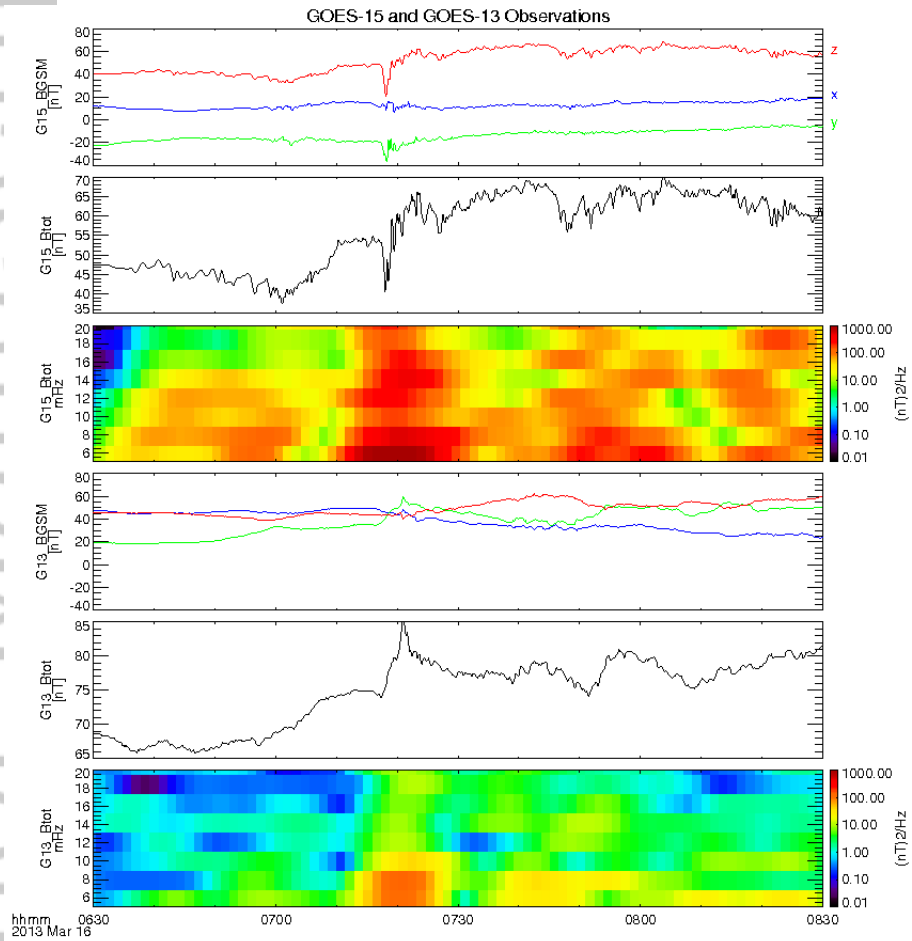
526 Finally, we examine in situ wave activity inside and immediately outside the plasma-
527 sphere using RBSP-B observations in Figure 11. During the period of interest, the RBSP-
528 B satellite was moving away from the Earth in the pre-midnight sector, at a similar lo-
529 cal time to the GOES-15 satellite (Figure 3A). The top panel of Figure 11 shows electron
530 density measured by RBSP-B as a black line, indicating that it crossed out of the high



471 **Figure 8.** Dynamic power spectra for BX measured at several ground magnetometer stations, all on the
 472 same scale and ordered according to magnetic latitude, with highest latitude at the top: FSIM, FTN, FSJ,
 473 PGEO, VIC, UKIA, CCNV, and FRN. The geomagnetic latitude for each station is indicated on the x-axis
 474 label.



500 **Figure 9.** The same as Figure 8 but for normalized dynamic power spectra to emphasize spectral features.
 501 At each time step, all power values from Figure 8 are divided all by the maximum power in the frequency
 502 range from 5 to 20 mHz. The geomagnetic latitude for each station is indicated on the x-axis label.



515 **Figure 10.** From top to bottom: (1) magnetic field measurement from GOES-15 in GSM coordinates, (2)
 516 total magnetic field measured by GOES-15, (3) dynamic power spectrum of GOES-15 total magnetic field
 517 perturbations, (4-6) the same as panels 1-3, but for GOES-13.

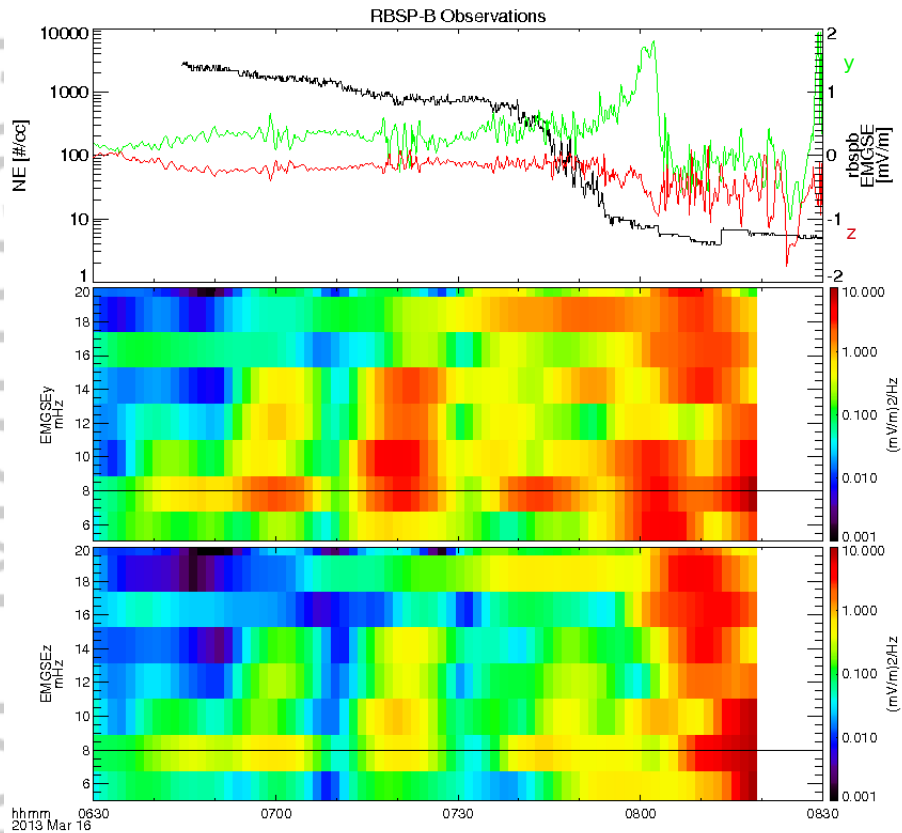
531 density plasmasphere at roughly 0750 UT. This panel also shows the unfiltered y (green)
532 and z (red) Modified Geocentric Solar Ecliptic (MGSE) components of the electric field.
533 In MGSE coordinates, x_{MGSE} points along the spacecraft spin axis and is usually close
534 to the x_{GSE} direction (Earth-Sun line), y_{MGSE} points along $z_{GSE} \times x_{MGSE}$ (in the spin
535 plane and ecliptic plane, close to the y_{GSE} /duskward direction), and z_{MGSE} completes
536 the right-handed orthogonal set, in the spin plane and close to the normal to the ecliptic
537 plane. The second panel of Figure 11 shows the dynamic power spectrum for the MGSE y
538 component of the electric field, while the third panel is for the z component. Both panels
539 indicate several periods with discrete frequency 8 mHz wave activity (e.g., 0640-0700 UT)
540 and periods with intensification of more broadband frequency wave activity that includes
541 8 mHz but peaks at other frequencies (e.g., 0720 UT). Upon crossing the plasmopause,
542 larger amplitude fluctuations are seen with a broader frequency spectrum, consistent with
543 GOES observations (Figure 10).

544 We also examined RBSP total magnetic field perturbations (not shown), finding
545 small amplitude perturbations and signals with 8 mHz frequency most clear during the
546 early part of the interval when RBSP is at lower L. If the 8 mHz signal is associated with
547 a PVR, the fact that it is most clear at low L may be related to the presence of a node
548 in magnetic field perturbations at spatial locations near the plasmopause, as reported in
549 previous PVR studies [Takahashi *et al.*, 2010]. Magnetic field perturbations in different
550 components also had small amplitudes and were dominated by the presence of an artificial
551 5-minute nutation signal (result of removing star tracker from spacecraft) during part of
552 the interval.

556 4 Discussion

557 In the previous section, we presented several observations of nightside Pi2 wave
558 properties during an extended period with stable plasmopause location and variable geo-
559 magnetic wave activity. To summarize observations from 0630-0830 UT on 16 Mar 2013:

- 560 1. Solar wind and geomagnetic activity: southward IMF and several sharp decreases
561 in AL for much of the early part of the day, then relatively quiet conditions in the
562 nightside magnetosphere at the beginning of the interval of interest until roughly
563 0716 UT when a substorm occurs and SAPS flows as large as 800 m/s develop.
- 564 2. Plasmopause location: Multiple satellite passes suggest the plasmopause location
565 does not change between 0630 and 0830 UT. The radial density profile also changes
566 little in the pre-midnight sector between the RBSP-B (0630-0845 UT) and RBSP-A
567 (0745-1030 UT) outbound passes. PTP simulations based on solar wind observa-
568 tions and the Kp index confirm this scenario.
- 569 3. Pi2 wave activity, latitudinal extent: 8 mHz signal is observed clearly by the RBSP-
570 B satellite when inside the plasmasphere. It is also observed by ground-based mag-
571 netometers at magnetic latitudes ranging from 41 to 67 degrees ($L=1.8$ to 6.6),
572 mapping to locations both inside and outside the plasmopause. Outside the plasma-
573 sphere, the 8 mHz signal may be obscured by larger amplitude wave activity with
574 a broadband frequency spectrum; for example, both RBSP-B and GOES satellites
575 observe Pi2 wave activity with a broader frequency spectrum outside the plasmas-
576 sphere, and the highest latitude FSIM ground station observes similar features during
577 later parts of the 0630-0830 UT interval.
- 578 4. Pi2 wave activity, longitudinal extent: Low latitude stations separated by 3.5 hours
579 MLT observe very similar 8 mHz wave forms with negligible time lags.
- 580 5. Pi2 wave activity, time evolution: 8 mHz signal is observed throughout the 0630-
581 0830 UT interval before, during, and after (1) the substorm, (2) other auroral inten-
582 sifications, (3) the development of SAPS flows, and (4) variations in the IMF. Wave
583 amplitudes vary in time at all locations and are strongest at the beginning of the
584 substorm.



553 **Figure 11.** From top to bottom: (1) RBSP-B electron density (black) and y (green) and z (red) compo-
 554 nents of the electric field in MGSE coordinates, (2) dynamic power spectrum for the electric field MGSE y
 555 component, (3) the same as 2 for the z component.

585 The 8 mHz wave observations are consistent with models of radially standing MHD fast
586 mode waves such as PVR: same frequency observed across a wide range of latitude/longitude,
587 frequency does not change through multiple intensifications as long as the radial den-
588 sity/Alfvén speed profile does not change, very small time lags between signals observed
589 at stations separated by 3.5 hours MLT suggest globally coherent wave activity with very
590 small (~ 0) azimuthal wave number, strong in situ electric field perturbations in conjunc-
591 tion with weak total magnetic field perturbations suggest nodal structure [*Li et al.*, 1998;
592 *Nosé et al.*, 2006; *Keiling and Takahashi*, 2011]. Phase differences between in situ electric
593 field and ground-based observations were also consistent with PVR during periods when
594 the RBSP-B electric field MGSE measurement was roughly aligned with the east-west di-
595 rection, and in situ and ground-based measurements had a high degree of coherence, con-
596 sistent with previous studies [*Takahashi et al.*, 2009]; for brevity sake we have not shown
597 these observations. We shall refer to these waves as a PVR rather than another standing
598 fast mode wave (e.g., plasmaspheric cavity mode) primarily due to observations in Figures
599 8 and 9 indicating the presence of monochromatic wave activity at latitudes mapping out-
600 side the plasmopause, particularly before 0700 UT. However, the distinction between PVR
601 and other standing fast mode waves is not important to the conclusions of this study, since
602 all such waves are sensitive to the radial density profile and plasmopause location.

603 Taken as a whole, the 8 mHz wave observations summarized above are also incon-
604 sistent with other Pi2 wave models. For example, Alfvén waves standing along the back-
605 ground magnetic field could not produce the same discrete frequency wave activity at dif-
606 ferent latitudes with no observable time lags (Figures 7 and 8). BBFs could not continu-
607 ously generate the same frequency wave activity throughout the entire two hour interval,
608 during both active and quiet conditions. However, with regard to the more broadband fre-
609 quency wave activity observed at higher latitudes, BBFs/plasma sheet flow bursts are a
610 plausible generation mechanism [e.g., *Nishimura et al.*, 2012; *Ream et al.*, 2015]. Finally,
611 the PGEO ground station close to the plasmopause (Figure 3B) observes locally enhanced
612 power at 8 mHz when compared to adjacent stations, suggestive of a plasmopause surface
613 wave. However, we can discard the plasmopause surface wave explanation in this study
614 based on the small phase differences between 8 mHz signals measured at longitudinally
615 separated stations (Figure 7), since such waves are expected to have large azimuthal wave
616 numbers [*Chen and Hasegawa*, 1974]. Instead, this feature may relate to (1) radial PVR
617 structure or field line resonances associated with radial density gradients at the plasma-
618 pause, (2) latitudinal ionospheric conductivity variations, or (3) a combination of (1) and
619 (2) [e.g., *Takahashi et al.*, 2003; *Keiling and Takahashi*, 2011; *Lysak et al.*, 2015; *Shi et al.*,
620 2017]. Identifying the source(s) of features such as these requires detailed comparisons
621 with numerical simulations and is thus an important topic for future work, and this study
622 provides important constraints for such simulations, including the radial density profile.

623 The stable radial plasma density profile and plasmopause location during variable
624 geomagnetic activity is a unique feature of this event. Since PVR properties depend strongly
625 on these factors, this event presents an opportunity to examine how other factors, such as
626 time variable external driving conditions (IMF, multiple BBFs, substorm) and ionospheric
627 boundary conditions (e.g., SAPS flows and accompanying conductivity variations) affect
628 PVR properties. In this event, we find that these other factors do not affect the PVR fre-
629 quency, as the 8 mHz signal is stable throughout the interval. By “stable” we mean that
630 the frequency of wave activity does not change from one wave intensification to the next,
631 within the accuracy of the DFT analysis. More specifically, the 256 point DFT analysis
632 shown in Figure 6, panel 8 indicates a persistent spectral feature with a frequency of 8.2
633 ± 0.53 mHz. The DFT window is 47 minutes long while the interval is two hours; thus,
634 the frequency of this feature obtained from DFT windows at the beginning of the interval
635 is the same as the frequency at the end of the interval, to within the frequency uncertainty
636 of the DFT analysis (see section 2 for more discussion of uncertainty). There are locations
637 and times when the 8.2 mHz signal is either not present or not detectable due to low am-

plitudes or the presence of other waves, but subsequent intensifications indicate a natural response frequency of the plasmasphere that does not change.

However, (external driving conditions and/or ionospheric variability) must play a role in the temporal and spatial variability of the PVR amplitude. These factors also affect other types of ULF wave activity that are important to the generation and detection of PVR. For example, waves with broadband frequency spectrum and large amplitudes were observed outside the plasmasphere in this study. These waves may be an energy source for the PVR while also obscuring the PVR from detection. In particular, the FSIM station observes significantly larger amplitude perturbations than other stations, and these perturbations tend to have a broadband frequency spectrum (Figure 8, panel 1). There are a few explanations for these features, not mutually exclusive: (1) radial PVR structure determined by the radial density profile, (2) high-latitude Pi2 waves that may act as an energy source of the PVR, such as flow bursts and related Alfvén waves occurring outside the plasmopause (see *Keiling and Takahashi* [2011] for additional high-latitude Pi2 models), (3) latitudinal variations in ionospheric conductivity that affect the amplitude of ground magnetic perturbations and the closure of magnetospheric currents. 1-3 could independently, or together, result in the differences seen at FSIM, and it is possible for a both PVR and other types of Pi2 waves to be observed simultaneously at FSIM's high-latitude location. Numerical simulations are beginning to resolve this type of ambiguity [e.g., *Lysak et al.*, 2015], but fully explaining the features seen at FSIM in the context of 1-3 is outside the scope of the present study.

Finally, we note that if we had only considered observations during a narrow time range near substorm onset or a limited spatial range (e.g., near SAPS flows or plasmopause location), we may well have associated the 8 mHz wave activity with BBFs, plasmopause surface waves, or another Pi2 model. This demonstrates the need for globally distributed observations and extended analysis periods when associating Pi2 wave observations with different wave sources, as noted by *Keiling and Takahashi* [2011].

5 Summary

The frequencies and amplitudes of Pi2 waves such as PVR are strongly affected by the plasmopause location. The present study extends previous work relating Pi2 wave activity to plasmopause location [e.g., *Takahashi et al.*, 2003, 2005; *Ghamry et al.*, 2015; *Shi et al.*, 2017] by examining wave activity during an extended interval with stable plasmopause location and variable geomagnetic activity. To summarize our key findings:

1. Multiple satellite passes and PTP simulations indicate the plasmopause location is stable for at least two hours over a wide range of MLT. This stability allows us to examine how other factors affect Pi2 wave properties.
2. Both in situ and ground-based measurements indicate multiple intensifications of a PVR through a period of variable geomagnetic activity. Other wave activity with a more broadband frequency spectrum also occurs, primarily outside the plasmopause.
3. PVR wave amplitudes vary spatially and temporally while frequency remains stable at 8.2 +/- 0.53 mHz, based on low latitude ground magnetometer observations. The frequency is stable throughout multiple wave intensifications that occur before, during, and after (1) a substorm, (2) multiple auroral intensifications, (3) the development of SAPS flows and associated ionospheric conductivity variations, and (4) variations in the IMF. The stable frequency is consistent with PVR model predictions - and other standing fast mode wave model predictions - for a stable plasmopause location.

Stable plasmopause locations are necessary for stable PVR frequencies. In this study, we found that a stationary plasmopause before, during, and after a substorm was likely

688 caused by a prolonged period of southward IMF preceding the interval of interest, during
689 which the plasmopause location changed and erosion occurred. We speculate that con-
690 ditions similar to those found in the present study - i.e., periods with substorms or other
691 Pi2 energy sources occurring after a significant erosion event - may be favorable for stable
692 PVR frequencies due to stable density conditions.

693 To better understand the spatial and temporal variability of Pi2 wave activity during
694 geomagnetically active periods, more work is needed to examine how wave properties vary
695 during periods with relatively stable plasmopause locations such as the one in the present
696 study. In particular, observational comparisons with global numerical simulations [e.g.,
697 *Lysak et al., 2015; Ream et al., 2015; Claudepierre et al., 2016*] during periods with stable
698 plasmopause location are needed to better characterize the role of other factors (e.g., spa-
699 tially varying ionospheric conductivity, time varying driving conditions) besides the radial
700 density profile in determining wave properties and understanding why PVR are excited
701 during some periods but not others [e.g., *Osaki et al., 1998; Nishimura et al., 2012*].

702 Acknowledgments

703 M.D. Hartinger was supported by NSF grant AGS-1342968 and NASA grant NNX17AD35G.
704 S. Zou was supported by NSF grant AGS-1342968. K. Takahashi was supported by NASA
705 grant NNX15AI95G. X. Shi was supported by NSF grant AGS-1341918. RBSP electron
706 density data used in this paper are available from <http://emfsis.physics.uiowa.edu>. The
707 research at University of Iowa was supported by JHU/APL contract 921647 under NASA
708 prime contract NAS5-01072. The work by the RBSP EFW team was conducted under
709 JHU/APL contract 922613 (RBSP-EFW). We acknowledge the use of SuperDARN Data
710 publicly available at <http://vt.superdarn.org/>. SuperDARN is a collection of radars funded
711 by national scientific funding agencies of Australia, Canada, China, France, Italy, Japan,
712 Norway, South Africa, United Kingdom and the United States. All ground magnetome-
713 ter data are publicly available at <http://themis.ssl.berkeley.edu/data/themis/thg/l2/mag/>. We
714 acknowledge the use of data collected at magnetic observatories operated by the U.S. Ge-
715 ological Survey (USGS, geomag.usgs.gov). We thank I.R. Mann, D.K. Milling and the
716 rest of the CARISMA team for data. CARISMA is operated by the University of Alberta,
717 funded by the Canadian Space Agency (<http://www.carisma.ca/>). We acknowledge NASA
718 contract NAS5-02099 and V. Angelopoulos for use of data from the THEMIS Mission.
719 Specifically: S. Mende and C. T. Russell for use of the GMAG data and NSF for support
720 through grant AGS-1004814; the Canadian Magnetic Observatory Network (CANMON)
721 maintained and operated by the Geological Survey of Canada (<http://www.geomag.nrcan.gc.ca/>);
722 Dr. Kanji Hayashi, University of Tokyo for use of magnetometer data from the Solar-
723 Terrestrial Energy Program Polar Network (<http://step-p.dyndns.org/~khay/>). We thank
724 the NASA Space Science Data facility for use of solar wind data and geomagnetic activity
725 indices. We thank Haje Korth for providing the Geopack interface as part of the SPEDAS
726 software package, and Kolya Tsyganenko for creating the Geopack library and external
727 field models. Magnetic field input parameters (derived from data on OMNIWeb) were pro-
728 vided by Richard Denton and Zhengui Qin. Data and the SPEDAS software package used
729 for this study can be obtained from the THEMIS website (themis.ssl.berkeley.edu/index.shtml,
730 software version r22843). We thank Aaron Breneman, Michael Ruohoniemi, and Scott
731 Bounds for useful discussions and data interpretation.

732 References

- 733 Anderson, P.C., W.B. Hanson, R.A. Heelis, J.D. Craven, D.N. Baker, and L.A. Frank
734 (1993), A proposed production model of rapid subauroral ion drifts and their relation-
735 ship to substorm evolution, *Journal of Geophysical Research*, 98, 6069-6078.
- 736 Archer, M.O., M.D. Hartinger, B.M. Walsh, and F. Plaschke (2015), Frequency variability
737 of standing Alfvén waves excited by fast mode resonances in the outer magnetosphere,
738 *Geophysical Research Letters*, 42, 10.

- 739 Archer, M.O., M.D. Hartinger, B.M. Walsh, and V. Angelopoulos (2017), Magnetospheric
740 and solar wind dependences of coupled fast-mode resonances outside the plasmasphere,
741 *Journal of Geophysical Research (Space Physics)*, *122*, 212-226.
- 742 Claudepierre, S.G., F.R. Toffoletto, and M. Wiltberger (2016), Global MHD modeling of
743 resonant ULF waves: Simulations with and without a plasmasphere, *Journal of Geo-*
744 *physical Research (Space Physics)*, *121*, 227-244.
- 745 Chen, L., and A. Hasegawa (1974), A theory of long-period magnetic pulsations: 2. Im-
746 pulse excitation of surface eigenmode, *Journal of Geophysical Research*, *79*, 1033-1037.
- 747 Foster, J. C., and H. B. Vo (2002), Average characteristics and activity dependence of the
748 subauroral polarization stream, *Journal of Geophysical Research (Space Physics)*, *107*.
- 749 Fujita, S., and T. Tanaka (2013), Possible generation mechanisms of the Pi2 pulsations
750 estimated from a global MHD simulation, *Earth Planets Space*, *65*.
- 751 Ghamry, E., K.-H. Kim, H.-J. Kwon, D.-H. Lee, J.-S. Park, J. Choi, K. Hyun, W.S. Kurth,
752 C. Kletzing, J.R. Wygant, and J. Huang (2015), Simultaneous Pi2 observations by the
753 Van Allen Probes inside and outside the plasmasphere, *Journal of Geophysical Research*
754 *(Space Physics)*, *120*, 4567-4575.
- 755 Goldstein, J., J.L. Burch, B.R. Sandel, S.B. Mende, P. C:Son Brandt, and M.R. Hairston
756 (2005), Coupled response of the inner magnetosphere and ionosphere on 17 April 2002,
757 *Journal of Geophysical Research (Space Physics)*, *110*, A03205.
- 758 Goldstein, J., S. De Pascuale, C. Kletzing, W. Kurth, K.J. Genestreti, R.M. Skoug, B.A.
759 Larsen, L.M. Kistler, C. Mouikis, and H. Spence (2014), Simulation of Van Allen
760 Probes plasmopause encounters, *Journal of Geophysical Research (Space Physics)*, *119*,
761 7464-7484.
- 762 Hartinger, M., M.B. Moldwin, V. Angelopoulos, K. Takahashi, H.J. Singer, R.R. Ander-
763 son, Y. Nishimura, and J.R. Wygant, J. R. (2010), Pc5 wave power in the quiet-time
764 plasmasphere and trough: CRRES observations, *Geophysical Research Letters*, *37*,
765 L07107.
- 766 Jacobs, J. A., Y. Kato, S. Matsushita, and V. A. Troitskaya (1964), Classification of Geo-
767 magnetic Micropulsations, *Journal of Geophysical Research*, *69*, 180-181.
- 768 Keiling, A., and K. Takahashi (2011), Review of Pi2 Models, *Space Science Reviews*, *161*,
769 63-148.
- 770 Kepko, L., M.G. Kivelson, and K. Yumoto (2001), Flow bursts, braking, and Pi2 pulsa-
771 tions, *Journal of Geophysical Research*, *106*, 1903-1916.
- 772 Kivelson, M. G., J. Etcheto, and J. G. Trotignon (1984), Global compressional oscillations
773 of the terrestrial magnetosphere - The evidence and a model, *Journal of Geophysical*
774 *Research*, *89*, 9851-9856.
- 775 Kletzing, C.A., W.S. Kurth, M. Acuna, R.J. MacDowall, R.B. Torbert, T. Averkamp, D.
776 Bodet, S.R. Bounds, M. Chutter, J. Connerney, D. Crawford, J.S. Dolan, R. Dvorsky,
777 G.B. Hospodarsky, J. Howard, V. Jordanova, R.A. Johnson, D.L. Kirchner, B. Mokrzy-
778 cki, G. Needell, J. Odom, D. Mark, R. Pfaff, J.R. Phillips, C.W. Piker, S.L. Remington,
779 D. Rowland, O. Santolik, R. Schnurr, D. Sheppard, C.W. Smith, R.M. Thorne, and J.
780 Tyler (2013), The Electric and Magnetic Field Instrument Suite and Integrated Science
781 (EMFISIS) on RBSP, *Space Science Reviews*, *179*, 127-181.
- 782 Kwon, H.-J., K.-H. Kim, G. Jee, J.-S. Park, H. Jin, and Y. Nishimura (2015), Plasmopause
783 location under quiet geomagnetic conditions ($K_p \leq 1$): THEMIS observations, *Geo-*
784 *physical Research Letters*, *42*, 7303-7310.
- 785 Kurth, W.S., S. De Pascuale, J.B. Faden, C.A. Kletzing, G.B. Hospodarsky, S. Thaller,
786 J.R. Wygant (2015), Electron densities inferred from plasma wave spectra obtained by
787 the Waves instrument on Van Allen Probes, *Journal of Geophysical Research (Space*
788 *Physics)*, *120*.
- 789 Laakso, H., and A. Pedersen (1998), Ambient Electron Density Derived from Differen-
790 tial Potential Measurements, *Washington DC American Geophysical Union Geophysical*
791 *Monograph Series*, *102*, 49.
- 792 Lee, D. H., and K. Kim (1999), Compressional MHD waves in the magnetosphere: A new

793 approach, *Journal of Geophysical Research (Space Physics)*, *104*, 12379–12386.
794 Li, Y., B.J. Fraser, F.W. Menk, D.J. Webster, and K. Yumoto (1998), Properties and
795 sources of low and very low latitude Pi2 pulsations, *Journal of Geophysical Research*,
796 *103*, 2343-2358.

797 Luo, H., G. Chen, A. Du, V. Angelopoulos, W. Xu, X. Zhao, and Y. Wang (2011),
798 THEMIS multipoint observations of Pi2 pulsations inside and outside the plasmasphere,
799 *Journal of Geophysical Research*, *116*, A12206.

800 Love, J. J., and C. A. Finn (2011), The USGS Geomagnetism Program and Its Role in
801 Space Weather Monitoring, *Space Weather*, *9*, S07001.

802 Lysak, R.L., Y. Song, M.D. Sciffer, and C.L. Waters (2015), Propagation of Pi2 pulsa-
803 tions in a dipole model of the magnetosphere, *Journal of Geophysical Research (Space*
804 *Physics)*, *120*, 355-367.

805 Mann, I. R., D. K. Milling, I. J. Rae, L. G. Ozeke, A. Kale, Z. C. Kale, K. R. Murphy,
806 A. Parent, M. Usanova, D. M. Pahud, E.-A. Lee, V. Amalraj, D. D. Wallis, V. An-
807 gelopoulos, K.-H. Glassmeier, C. T. Russell, H.-U. Auster, and H. J. Singer (2008), The
808 Upgraded CARISMA Magnetometer Array in the THEMIS Era, *Space Science Reviews*,
809 *141*, 413–451.

810 Mauk, B.H. N.J. Fox, S.G. Kanekal, R.L. Kessel, D.G. Sibeck, and A. Ukhorskiy (2012),
811 Science Objectives and Rationale for the Radiation Belt Storm Probes Mission, *Space*
812 *Science Reviews*, *179*, 3–27, doi:10.1007/s11214-012-9908-y.

813 McFadden, J. P., C. W. Carlson, D. Larson, M. Ludlam, R. Abiad, B. Elliott, P. Turin,
814 M. Marckwordt, and V. Angelopoulos (2008), The THEMIS ESA Plasma Instrument
815 and In-flight Calibration, *Space Science Reviews*, *141*, 277–302.

816 Mende, S.B., S.E. Harris, H.U. Frey, V. Angelopoulos, C.T. Russell, E. Donovan, B.
817 Jackel, M. Greffen, and L.M. Peticolas (2008), The THEMIS Array of Ground-based
818 Observatories for the Study of Auroral Substorms, *Space Science Reviews*, *141*, 357–
819 387, doi:10.1007/s11214-008-9380-x.

820 Murakami, G., M. Hirai, and I. Yoshikawa (2007), The plasmopause response to the
821 southward turning of the IMF derived from sequential EUV images, *Journal of Geo-*
822 *physical Research (Space Physics)*, *112*, A06217, doi:10.1029/2006JA012174.

823 Nishimura, Y., L.R. Lyons, T. Kikuchi, V. Angelopoulos, E. Donovan, S. Mende, P.J. Chi,
824 and T. Nagatsuma (2012), Formation of substorm Pi2: A coherent response to auroral
825 streamers and currents, *Journal of Geophysical Research (Space Physics)*, *117*, A09218.

826 Nosé, M., K. Liou, and P.R. Sutcliffe (2008), Longitudinal dependence of characteristics
827 of low-latitude Pi2 pulsations observed at Kakioka and Hermanus, *Earth, Planets, and*
828 *Space*, *58*, 775-783.

829 Nosé, M. (2010), Excitation mechanism of low-latitude Pi2 pulsations: Cavity mode res-
830 onance or BBF-driven process?, *Journal of Geophysical Research (Space Physics)*, *115*,
831 A07221.

832 Onsager, T., R. Grubb, J. Kunches, L. Matheson, D. Speich, R.W. Zwickl, and H. Sauer
833 (1996), Monitoring space weather with the GOES magnetometers, in *Society of Photo-*
834 *Optical Instrumentation Engineers (SPIE) Conference Series*, *Society of Photo-Optical*
835 *Instrumentation Engineers (SPIE) Conference Series*, vol. 2812, edited by E. R. Wash-
836 well, pp. 281–290.

837 Osaki, H., K. Takahashi, H. Fukunishi, T. Nagatsuma, H. Oya, A. Matsuoka, and D.K.
838 Milling (1998), Pi2 pulsations observed from the Akebono satellite in the plasmasphere,
839 *Journal of Geophysical Research (Space Physics)*, *103*, 17605-17616.

840 Ream, J.B., R.J. Walker, M. Ashour-Abdalla, M. El-Alaoui, M. Wiltberger, M.G. Kivelson,
841 and M.L. Goldstein (2015), Propagation of Pi2 pulsations through the braking region in
842 global MHD simulations, *Journal of Geophysical Research (Space Physics)*, *120*, 10.

843 Redmon, R.J., J.V. Rodriguez, J.C. Green, D. Ober, G. Wilson, D. Knipp, L. Kilcommons,
844 and R. McGuire (2015), Improved Polar and Geosynchronous Satellite Data Sets Avail-
845 able in Common Data Format at the Coordinated Data Analysis Web, *Space Weather*,
846 *13*, 254-256.

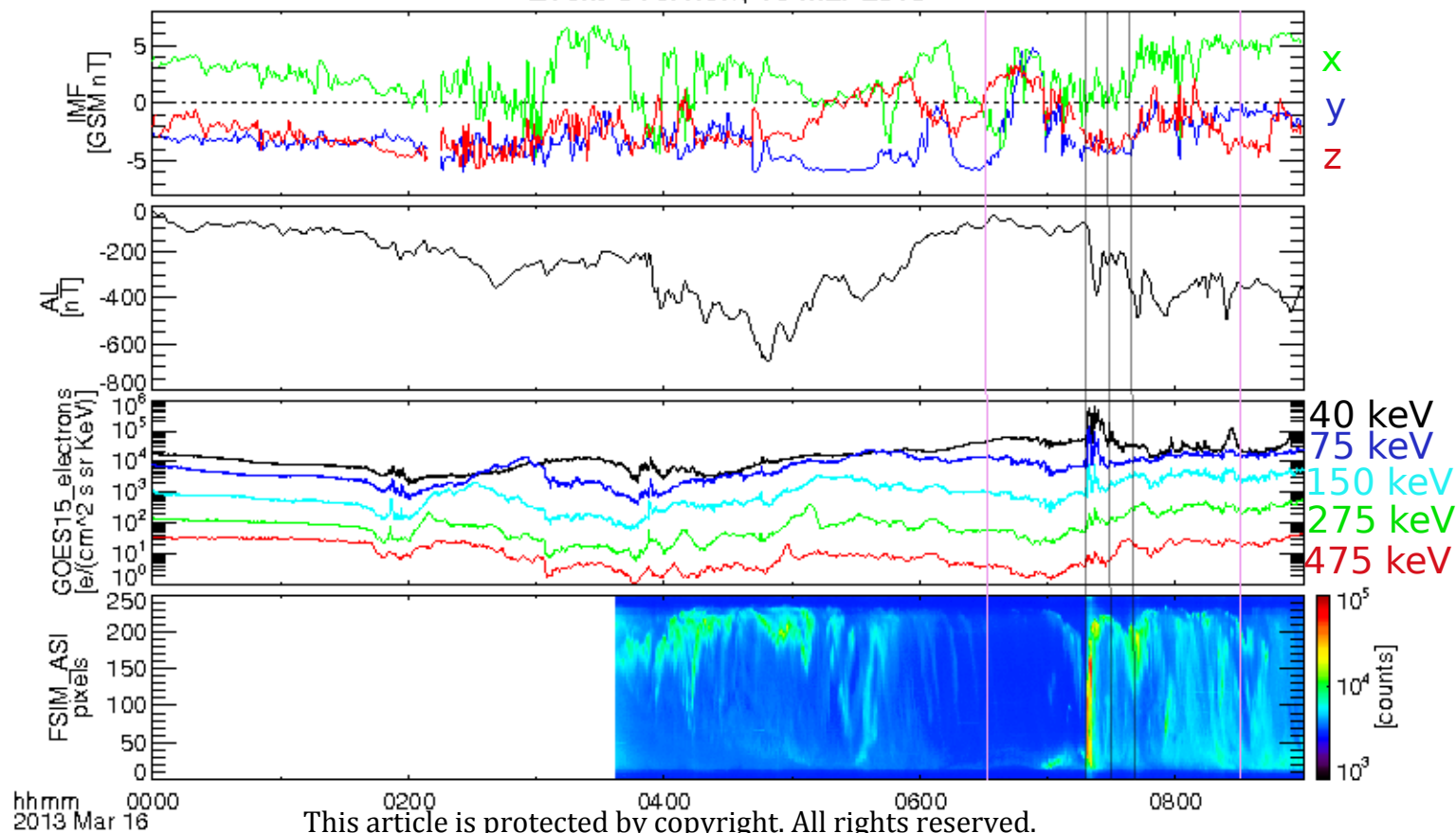
- 847 Rodriguez, J.V. (2014), GOES 13-15 MAGE/PD Pitch Angles Algorithm Theoretical Basis
848 Document, version 1.0, 28 pp., *NOAA National Geophysical Data Center*, [Available at
849 <http://www.ngdc.noaa.gov/stp/satellite/goes/documentation.html>].
- 850 Ruohoniemi, J.M., and K.B. Baker (1998), Large-scale imaging of high-latitude convection
851 with Super Dual Auroral Radar Network HF radar observations, *Journal of Geophysical*
852 *Research*, *103*, 20797-20811.
- 853 Russell, C. T., P. J. Chi, D. J. Dearborn, Y. S. Ge, B. Kuo-Tiong, J. D. Means, D. R.
854 Pierce, K. M. Rowe, and R. C. Snare (2008), THEMIS Ground-Based Magnetometers,
855 *Space Science Reviews*, *141*, doi:10.1007/s11214-008-9337-0.
- 856 Shi, X., J.B.H. Baker, J.M. Ruohoniemi, M.D. Hartinger, N.A. Friswell, and J. Liu (2017),
857 Simultaneous Space and Ground-Based Observations of a Plasmaspheric Virtual Reso-
858 nance, *Journal of Geophysical Research (Space Physics)*, *122*.
- 859 Sibeck, D. G., and V. Angelopoulos (2008), THEMIS Science Objectives and Mission
860 Phases, *Space Science Reviews*, *141*, 35–59.
- 861 Singer, H., L. Matheson, R. Grubb, A. Newman, and D. Bouwer (1996), Monitoring space
862 weather with the GOES magnetometers, in *Society of Photo-Optical Instrumentation*
863 *Engineers (SPIE) Conference Series, Society of Photo-Optical Instrumentation Engineers*
864 *(SPIE) Conference Series*, vol. 2812, edited by E. R. Washwell, pp. 299–308.
- 865 Takahashi, K., D.-H. Lee, M. Nosé, R.R. Anderson, and W.J. Hughes (2003), CRRES
866 electric field study of the radial mode structure of Pi2 pulsations, *Journal of Geophys-*
867 *ical Research*, *108*, 1210.
- 868 Takahashi, K., K. Liou, K. Yumoto, K. Kitamura, M. Nosé, and F. Honary (2005), Source
869 of Pc4 pulsations observed on the nightside, *Journal of Geophysical Research (Space*
870 *Physics)*, *110*, A12207.
- 871 Takahashi, K., D. Berube, D.-H. Lee, J. Goldstein, H.J. Singer, F. Honary, and M.B.
872 Moldwin (2009), Possible evidence of virtual resonance in the dayside magnetosphere,
873 *Journal of Geophysical Research (Space Physics)*, *114*, A05206.
- 874 Takahashi, K., J. Bonnell, K.-H. Glassmeier, V. Angelopoulos, H.J. Singer, P.J. Chi, R.E.
875 Denton, Y. Nishimura, D.-H. Lee, M. Nosé, and W. Liu (2010), Multipoint observation
876 of fast mode waves trapped in the dayside magnetosphere, *Journal of Geophysical Re-*
877 *search (Space Physics)*, *115*, A12247.
- 878 Teramoto, M., K. Takahashi, M. Nosé, D.-H. Lee, and P.R. Sutcliffe (2011), Pi2 pulsations
879 in the inner magnetosphere simultaneously observed by the Active Magnetospheric Par-
880 ticle Tracer Explorers/Charge Composition Explorer and Dynamics Explorer 1 satellites,
881 *Journal of Geophysical Research (Space Physics)*, *116*, A07225.
- 882 Tsyganenko, N. A. (1989), A magnetospheric magnetic field model with a warped tail cur-
883 rent sheet, *Planetary and Space Science*, *37*, 5–20.
- 884 Worthington, E.W., E.A. Sauter, and J.J. Love (2009), Analysis of USGS one-second data,
885 in *Proc. XIII IAGA Workshop*, (ed. J.J. Love), 262-266.
- 886 Wygant, J.R., J.W. Bonnell, K. Goetz, R.E. Ergun, F.S. Mozer, S.D. Bale, M. Ludlam, P.
887 Turin, P.R. Harvey, R. Hochmann, K. Harps, G. Dalton, J. McCauley, W. Rachelson, D.
888 Gordon, B. Donakowski, C. Shultz, C. Smith, M. Diaz-Aguado, J. Fischer, S. Heavner,
889 P. Berg, D.M. Malsapina, M.K. Bolton, M. Hudson, R.J. Strangeway, D.N. Baker, X. Li,
890 J. Albert, J.C. Foster, C.C. Chaston, I. Mann, E. Donovan, C.M. Cully, C.A. Cattell, V.
891 Krasnoselskikh, K. Kersten, A. Brennenman, and J.B. Tao (2013), The Electric Field and
892 Waves Instruments on the Radiation Belt Storm Probes Mission, *Space Science Reviews*,
893 *179*, 183–220, doi:10.1007/s11214-013-0013-7.
- 894 Zou, S., L.R. Lyons, C.-P. Wang, A. Boudouridis, J.M. Ruohoniemi, P.C. Anderson, P.L.
895 Dyson, and J.C. Devlin (2009a), On the coupling between the Harang reversal evolution
896 and substorm dynamics: a synthesis of SuperDARN, DMSP and IMAGE observations,
897 *Journal of Geophysical Research*, *114*, A01205, doi:10.1029/2008JA013449.
- 898 Zou, S., L.R. Lyons, M.J. Nicolls, C.J. Heinselman, and S.B. Mende (2009b), Nightside
899 ionospheric electrodynamics associated with substorms: PFISR and THEMIS ASI ob-
900 servations, *Journal of Geophysical Research*, *114*, A12301, doi:10.1029/2009JA014259.

901 Zou, S., L. Lyons, and Y. Nishimura (2012), Mutual Evolution of Aurora and Ionospheric
902 Electrodynamic Features Near the Harang Reversal During Substorms, in *Auroral Phenomenology and Magnetospheric Processes: Earth And Other Planets*, (eds A. Keiling,
903 E. Donovan, F. Bagenal and T. Karlsson), *American Geophysical Union*, Washington
904 D.C., doi:10.1029/2011GM001163.
905

Author Manuscript

Author Manuscript

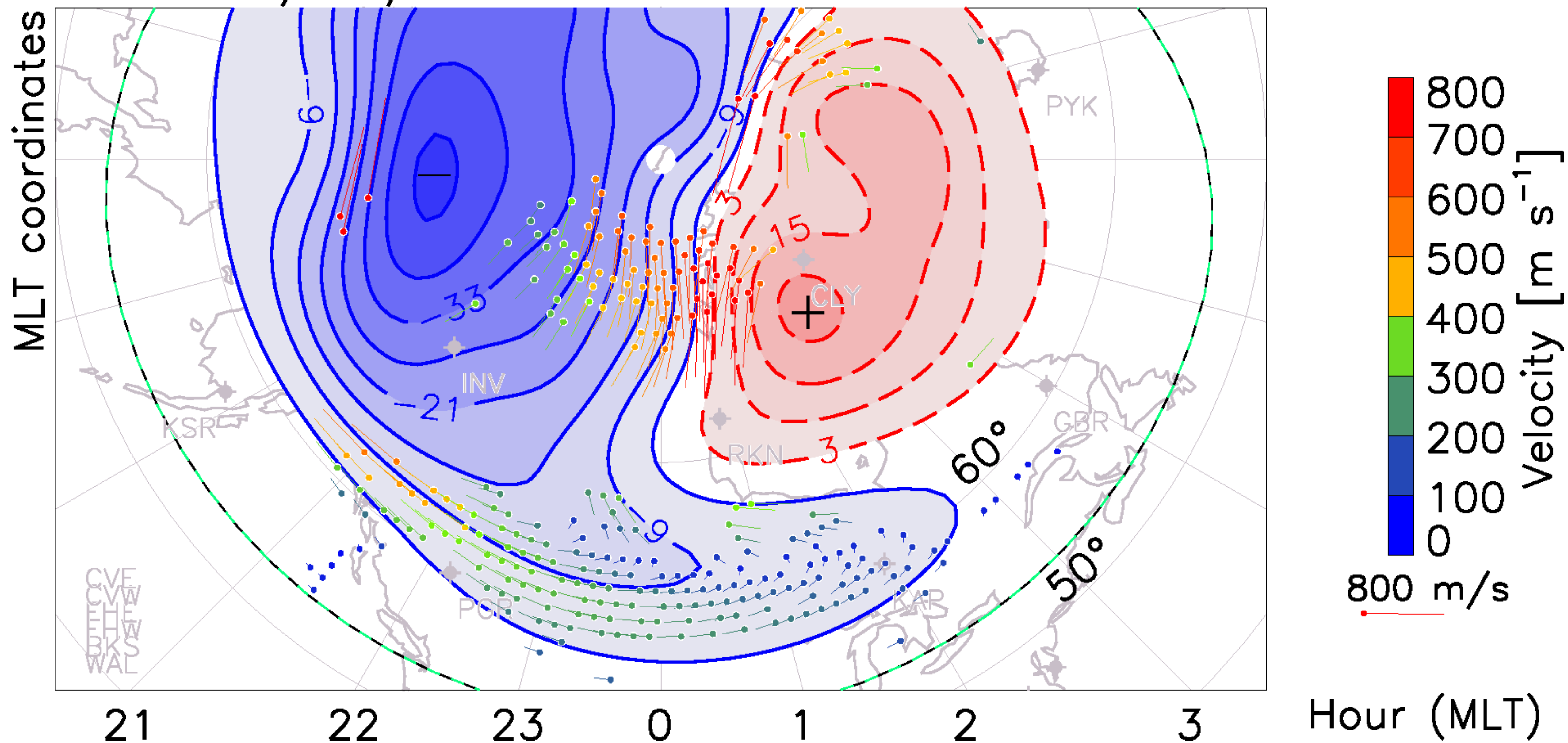
Event Overview, 16 Mar 2013



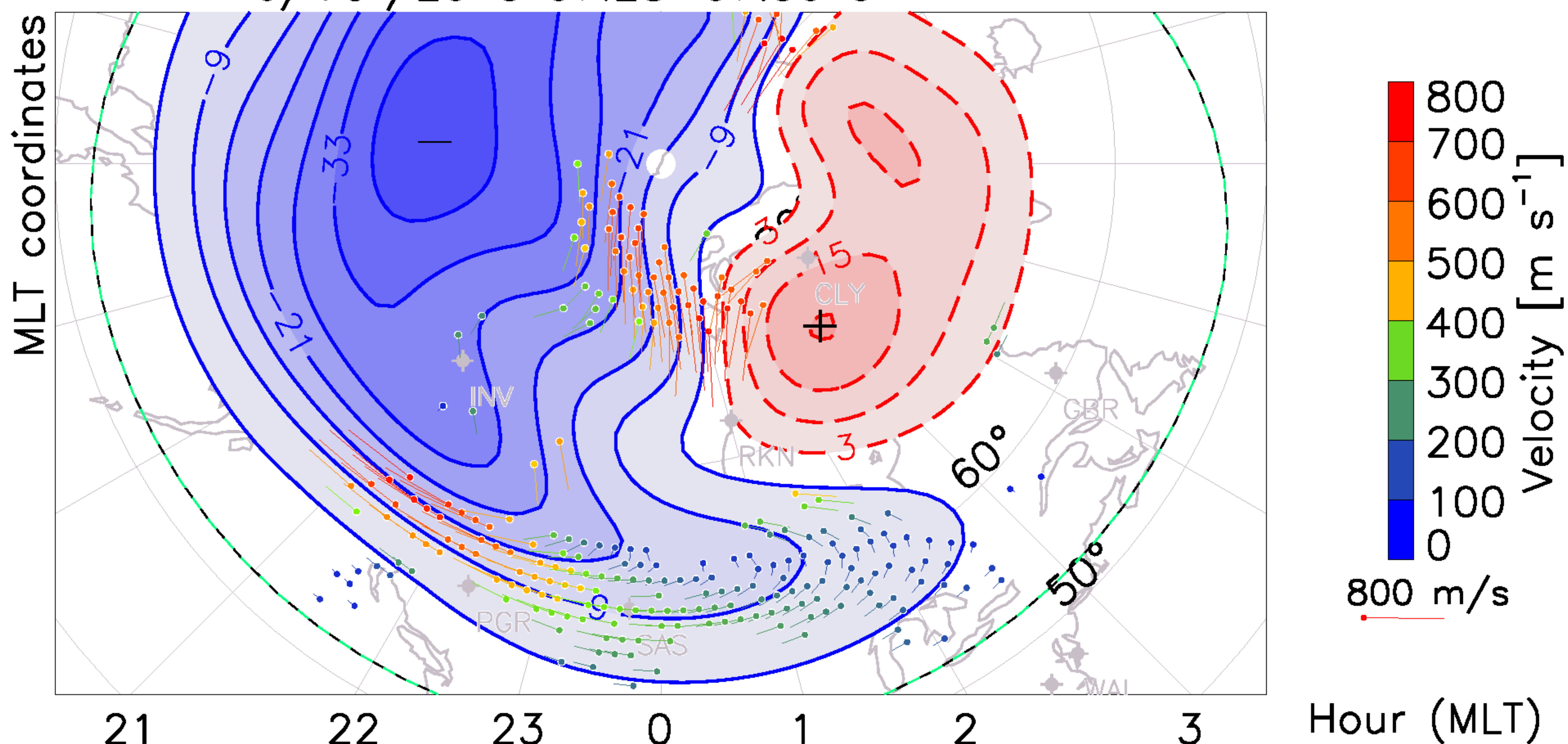
This article is protected by copyright. All rights reserved.

Author Manuscript

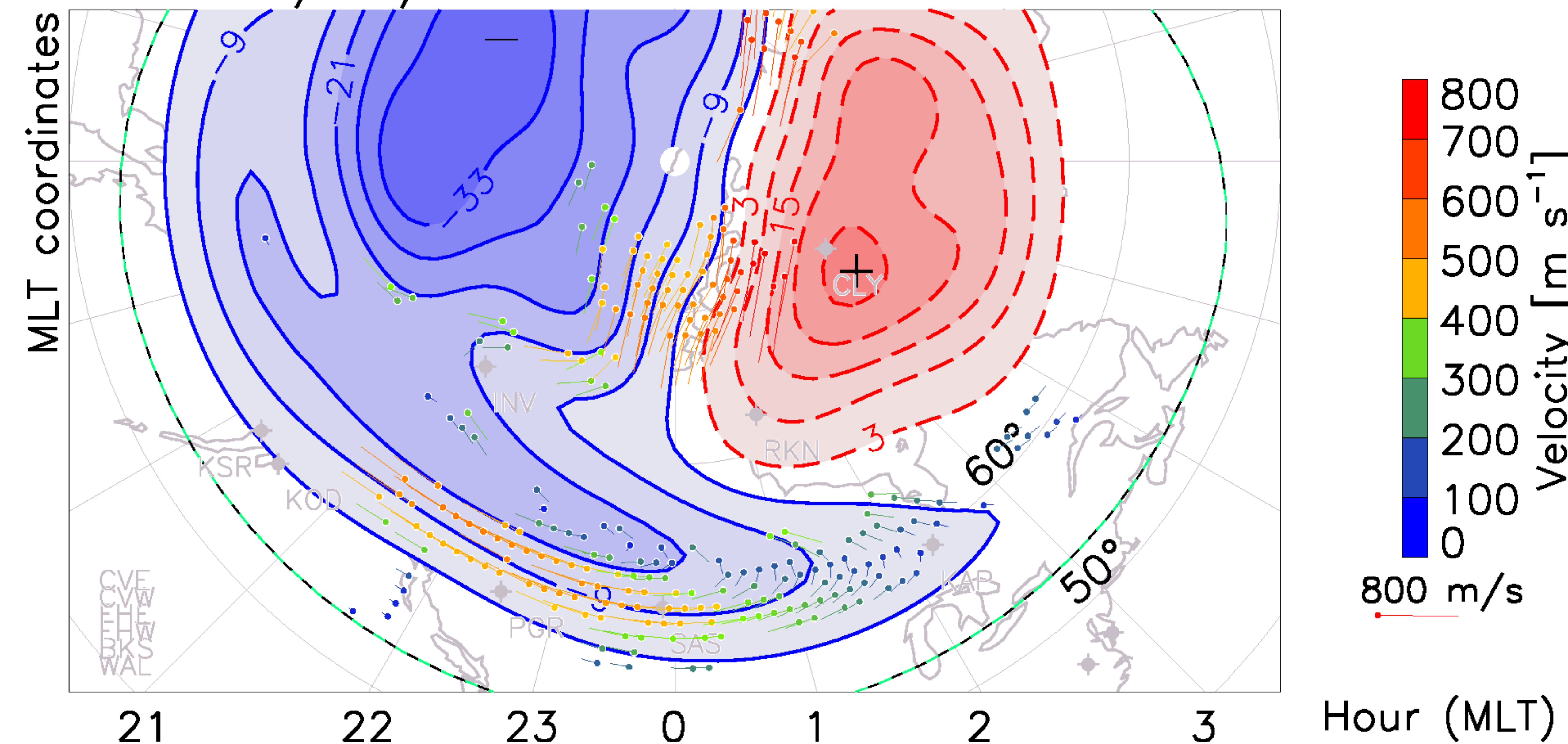
16/Mar/2013 07:18-07:20 UT



16/Mar/2013 07:28-07:30 UT



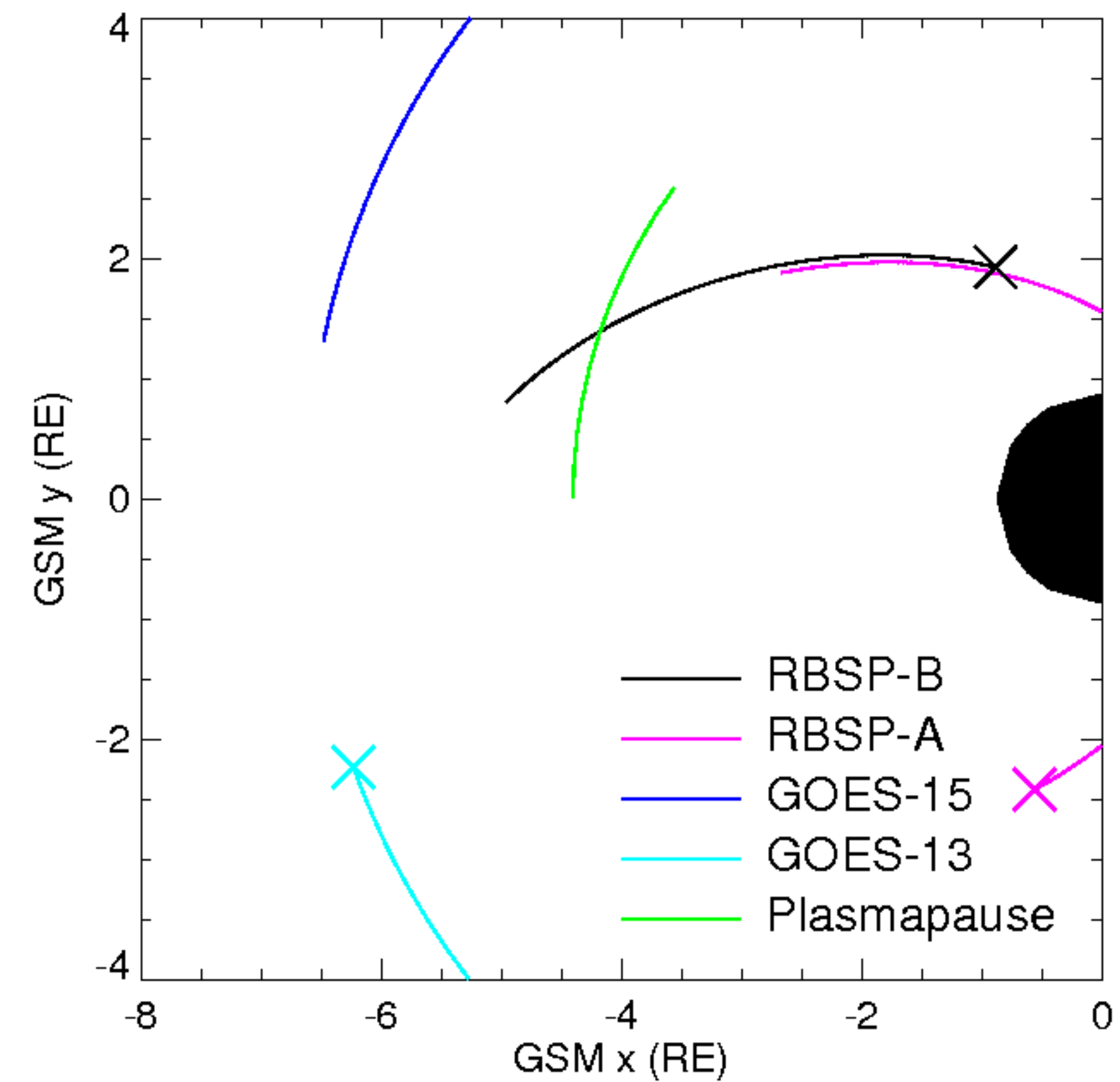
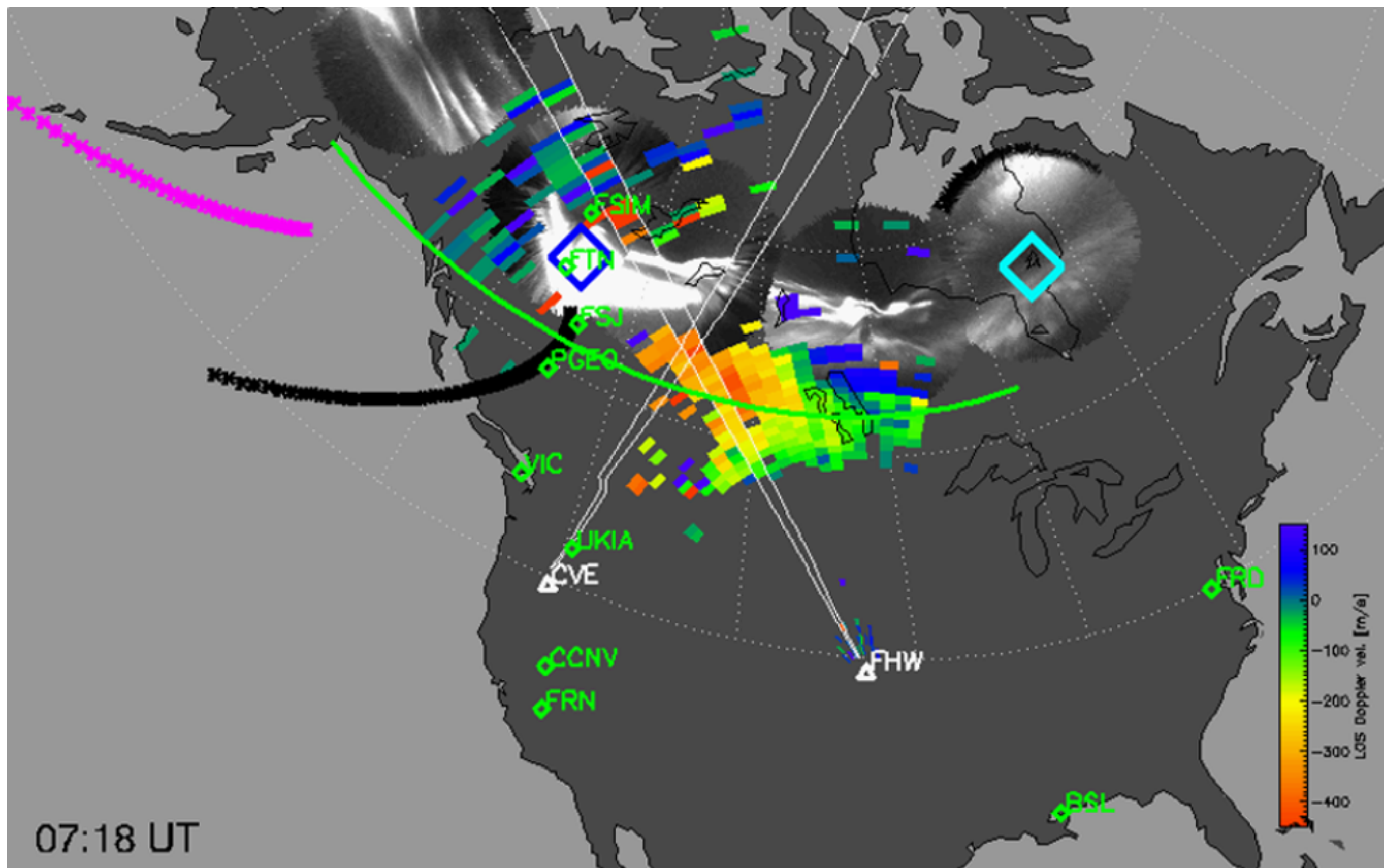
16/Mar/2013 07:38-07:40 UT



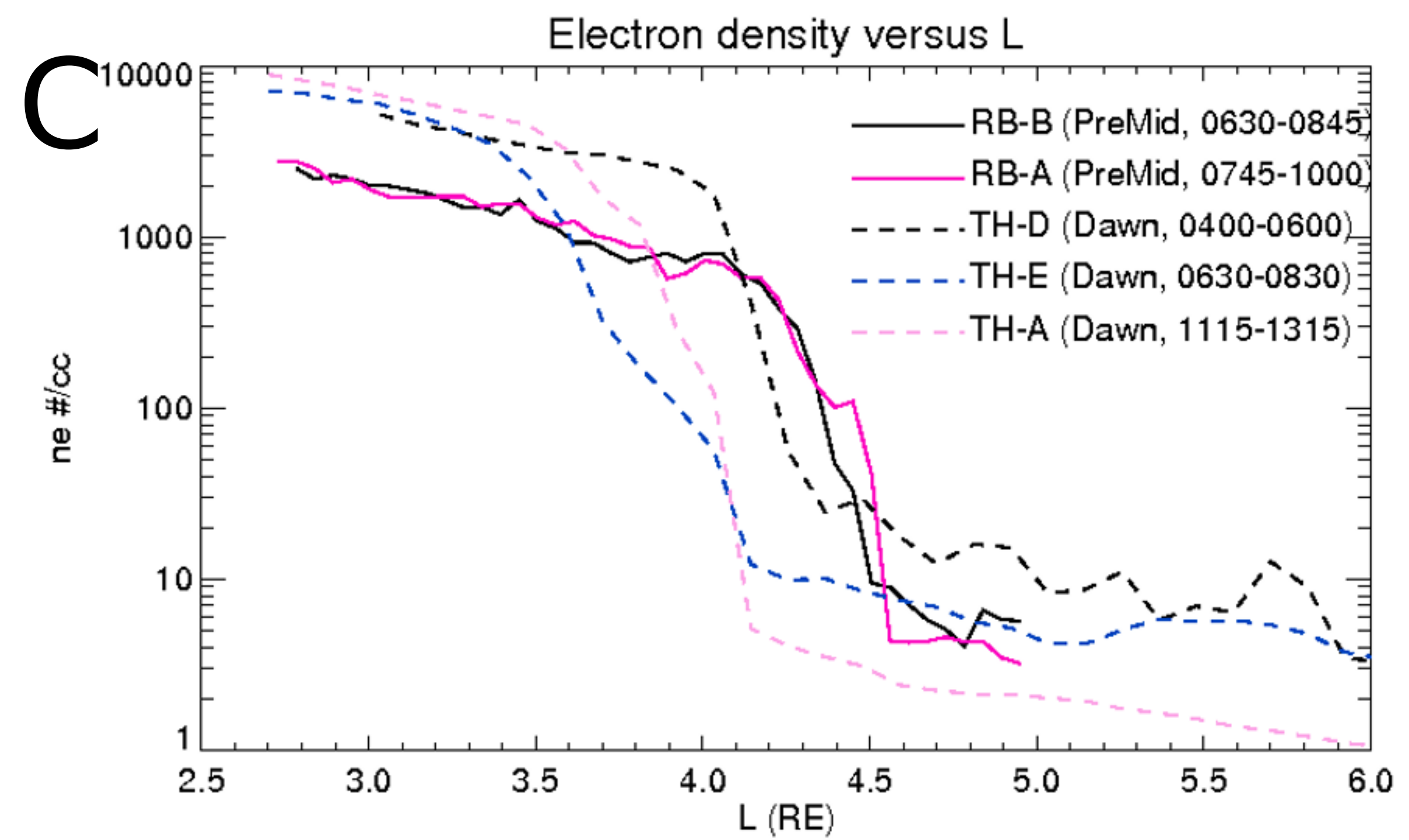
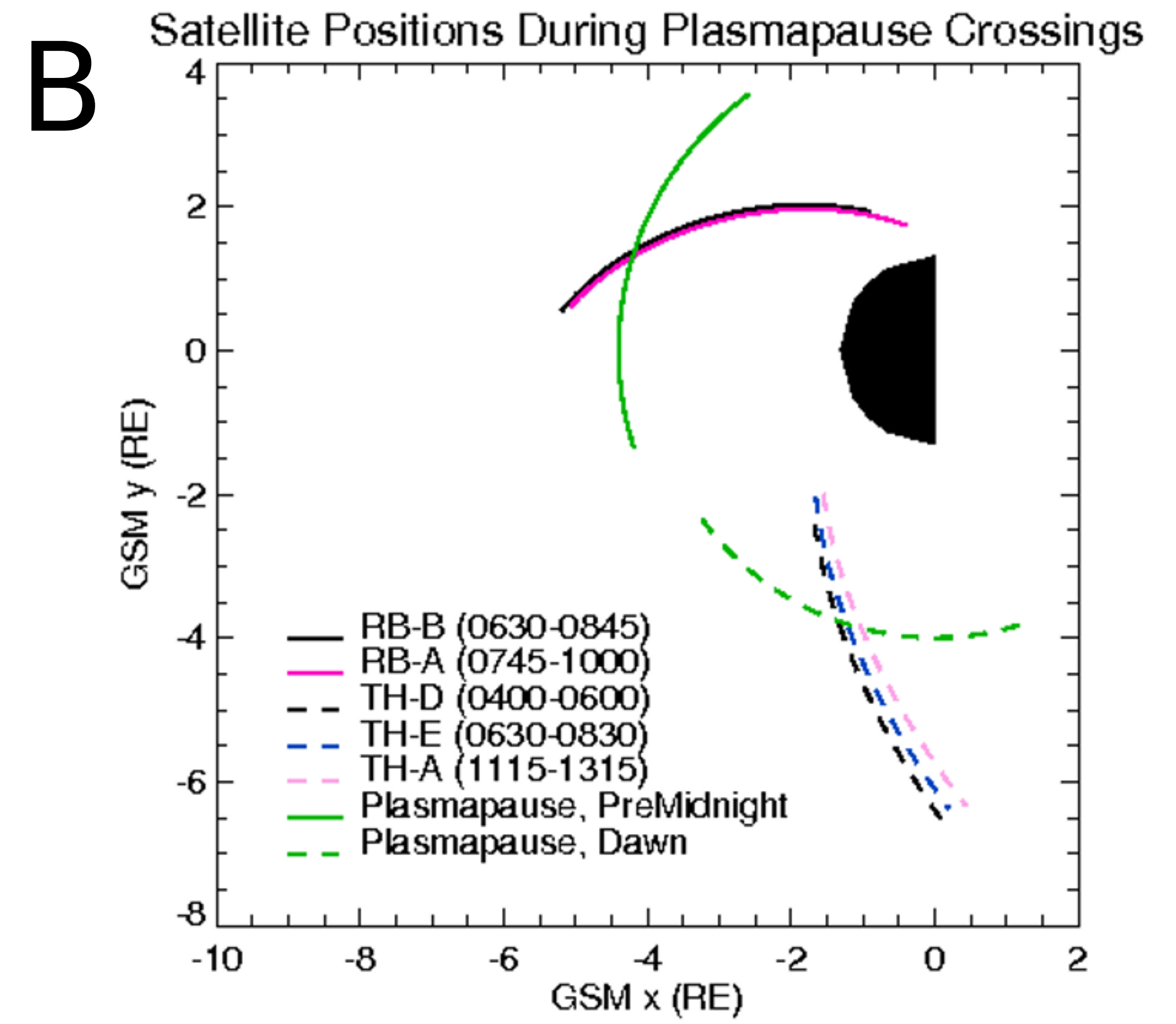
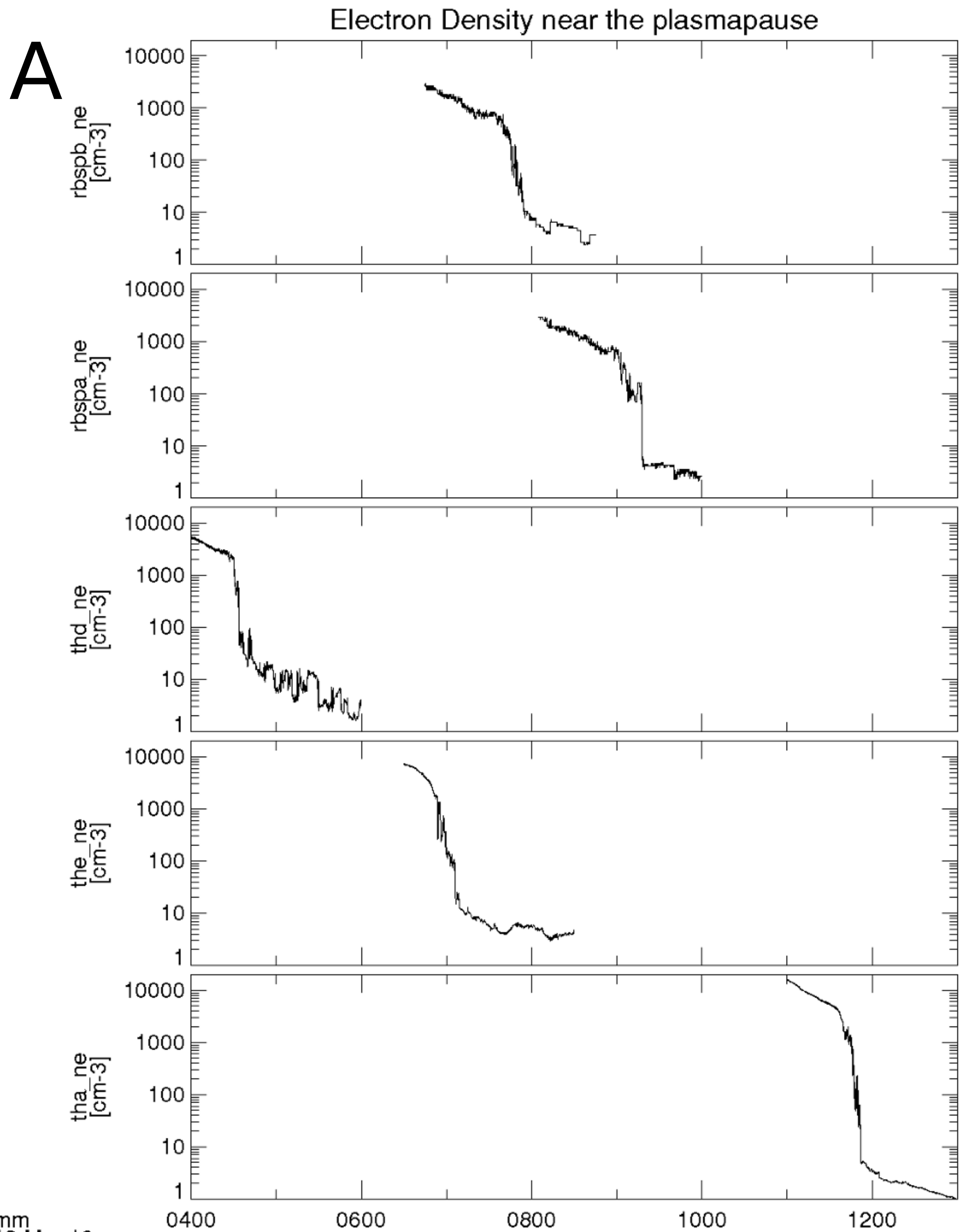
Author Manuscript

A

Satellite Positions 0630-0830 UT

**B**

Author Manuscript



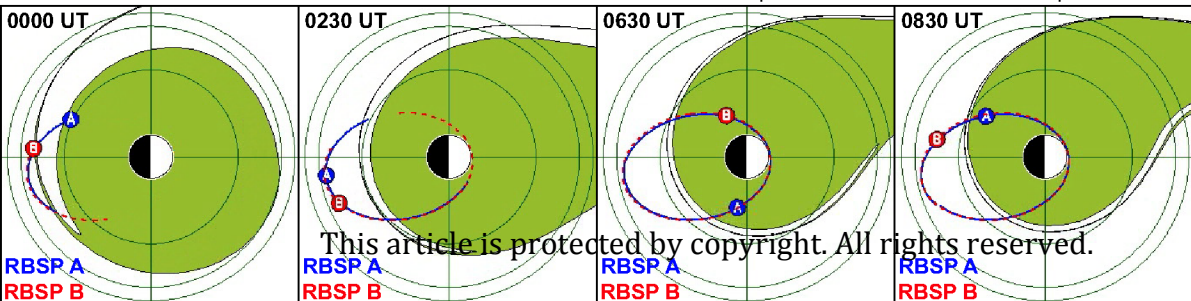
Author Manuscript

(a) Start of day

(b) Erosion in progress

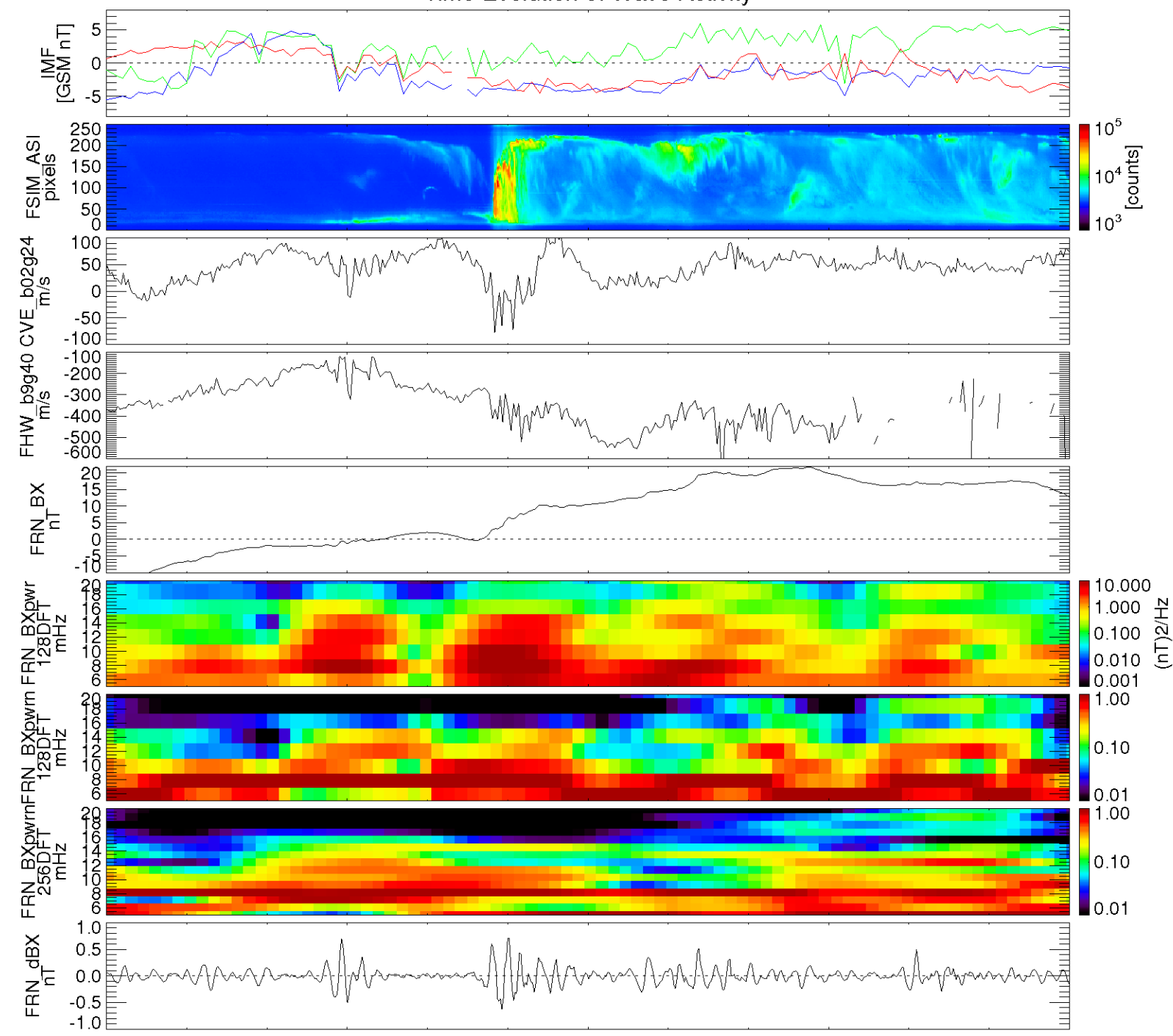
(c) Stable Nightside
Plasmapause

(d) Stable Nightside
Plasmapause



Author Manuscript

Time Evolution of Wave Activity



hhmm 0630
2013 Mar 16

0700
This article is protected by copyright. All rights reserved.

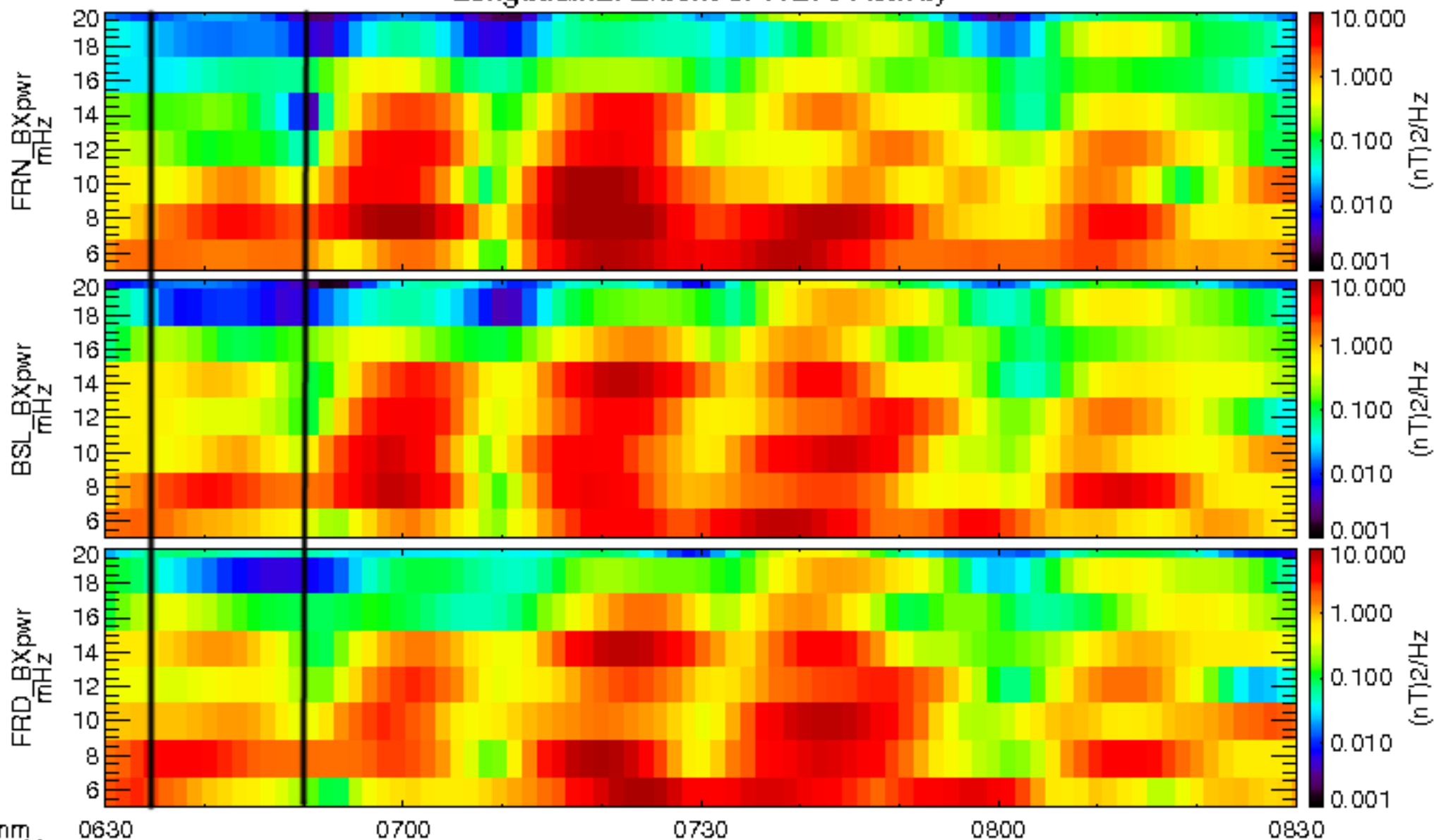
0730

0800

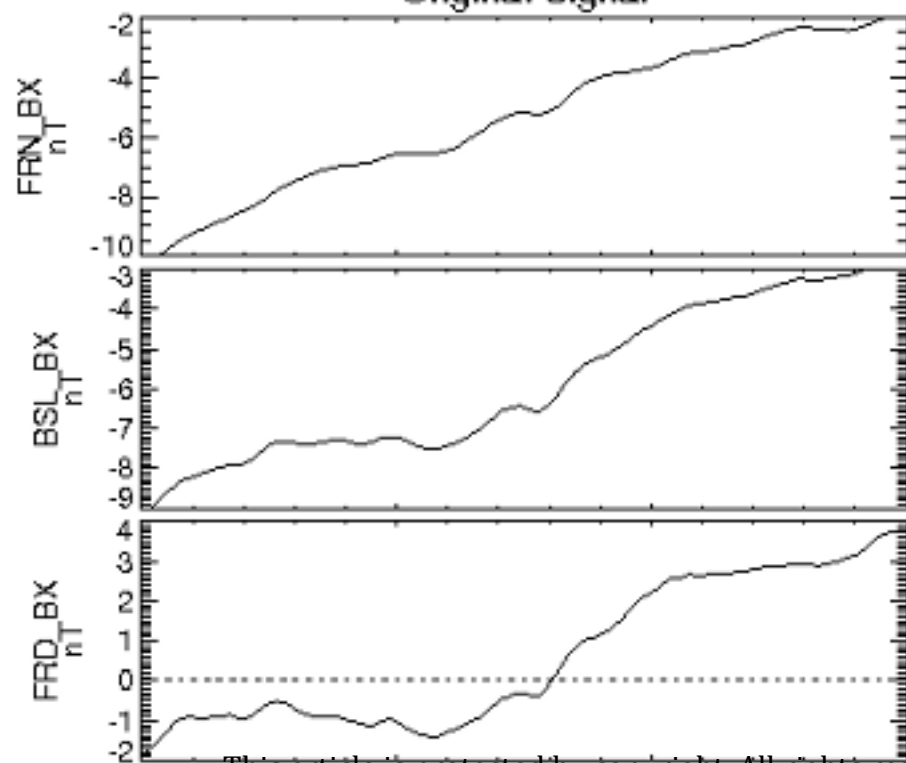
0830

Author Manuscript

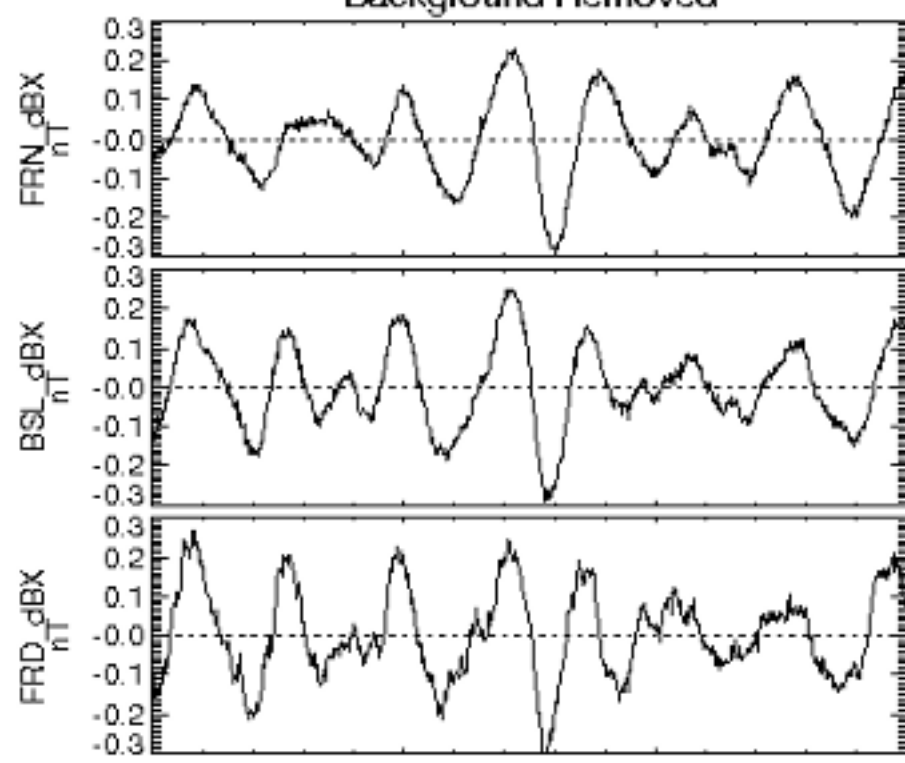
Longitudinal Extent of Wave Activity



Original Signal

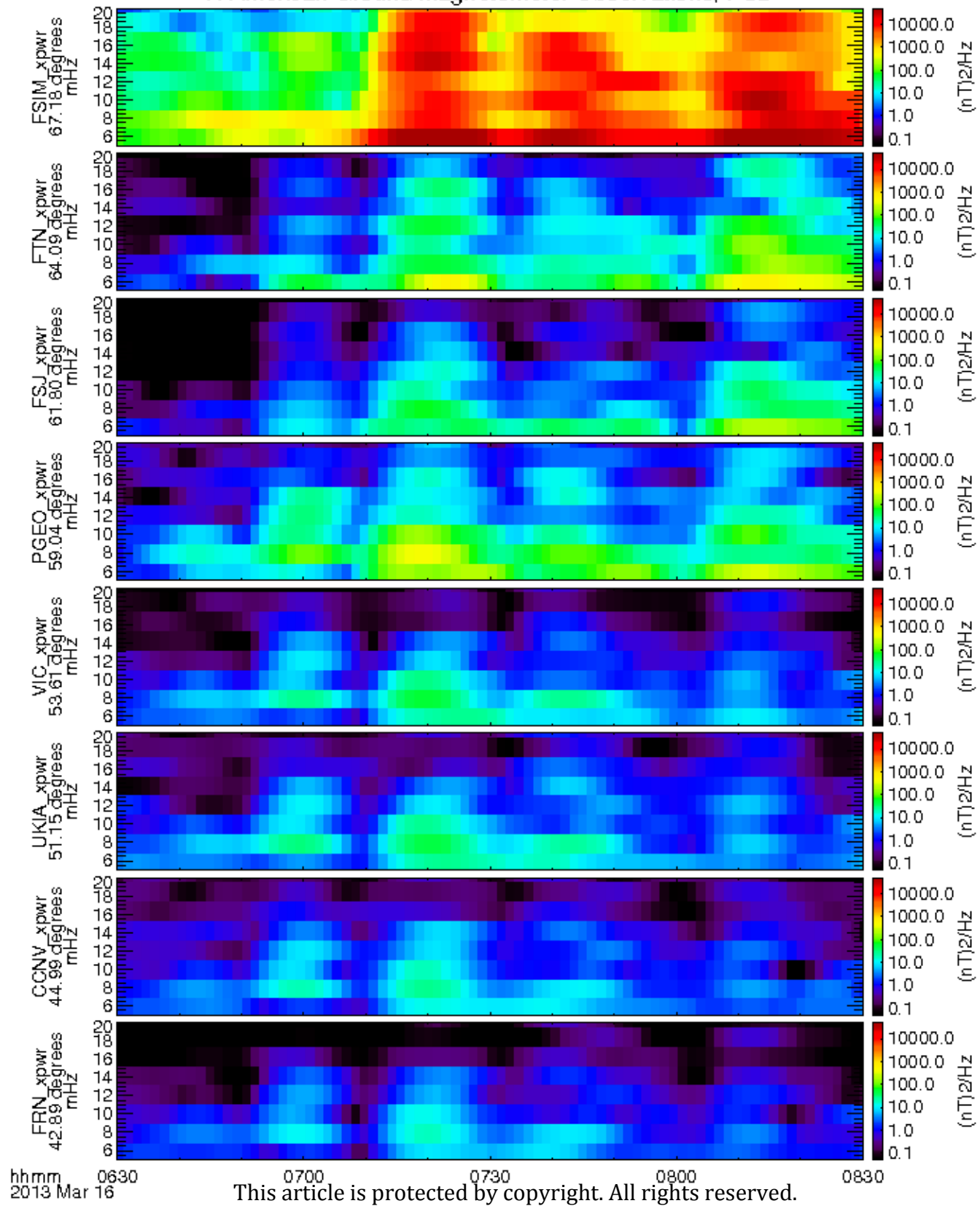


Background Removed



Author Manuscript

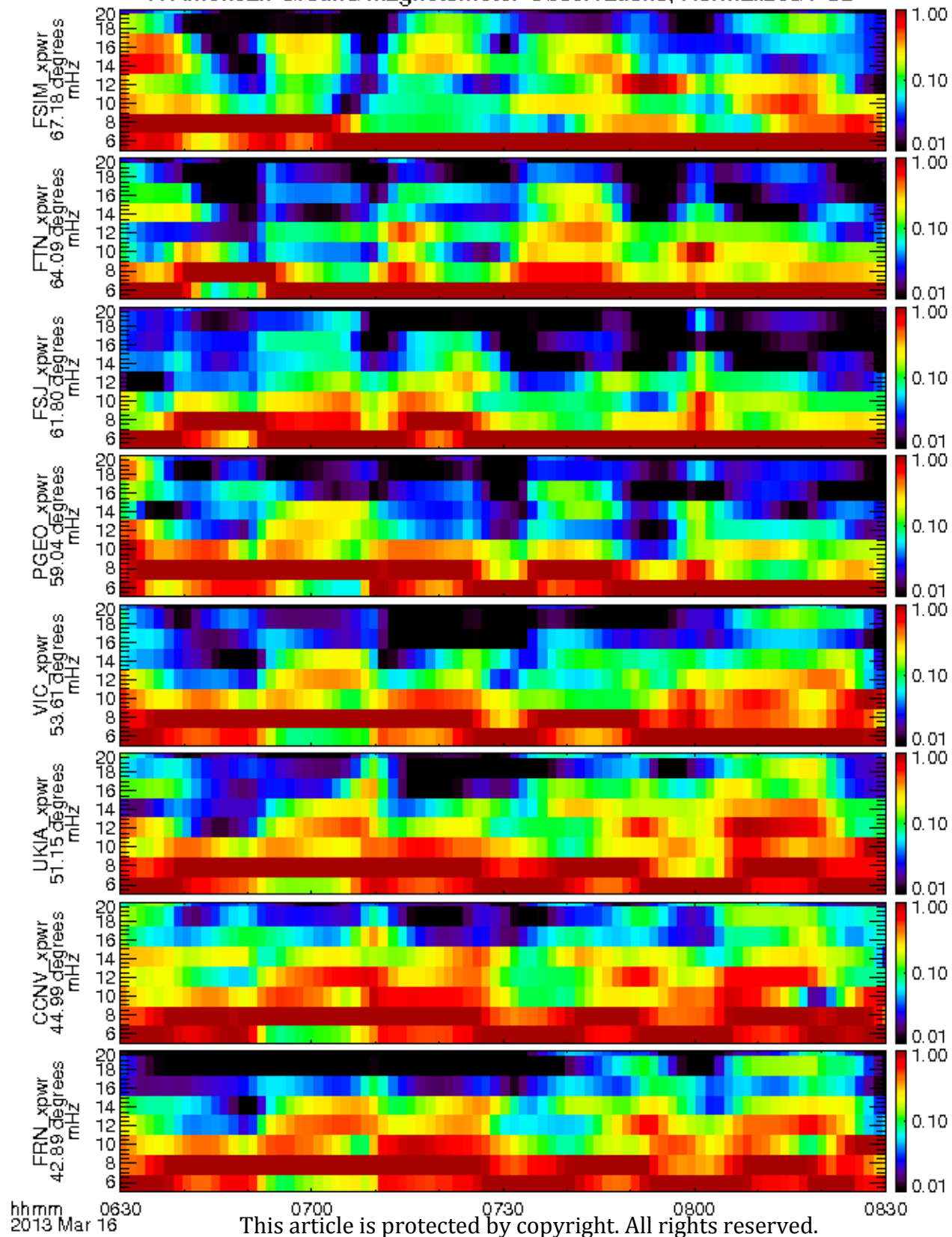
N American Ground Magnetometer Observations, PSD



hh mm
2013 Mar 16

Author Manuscript

N American Ground Magnetometer Observations, Normalized PSD

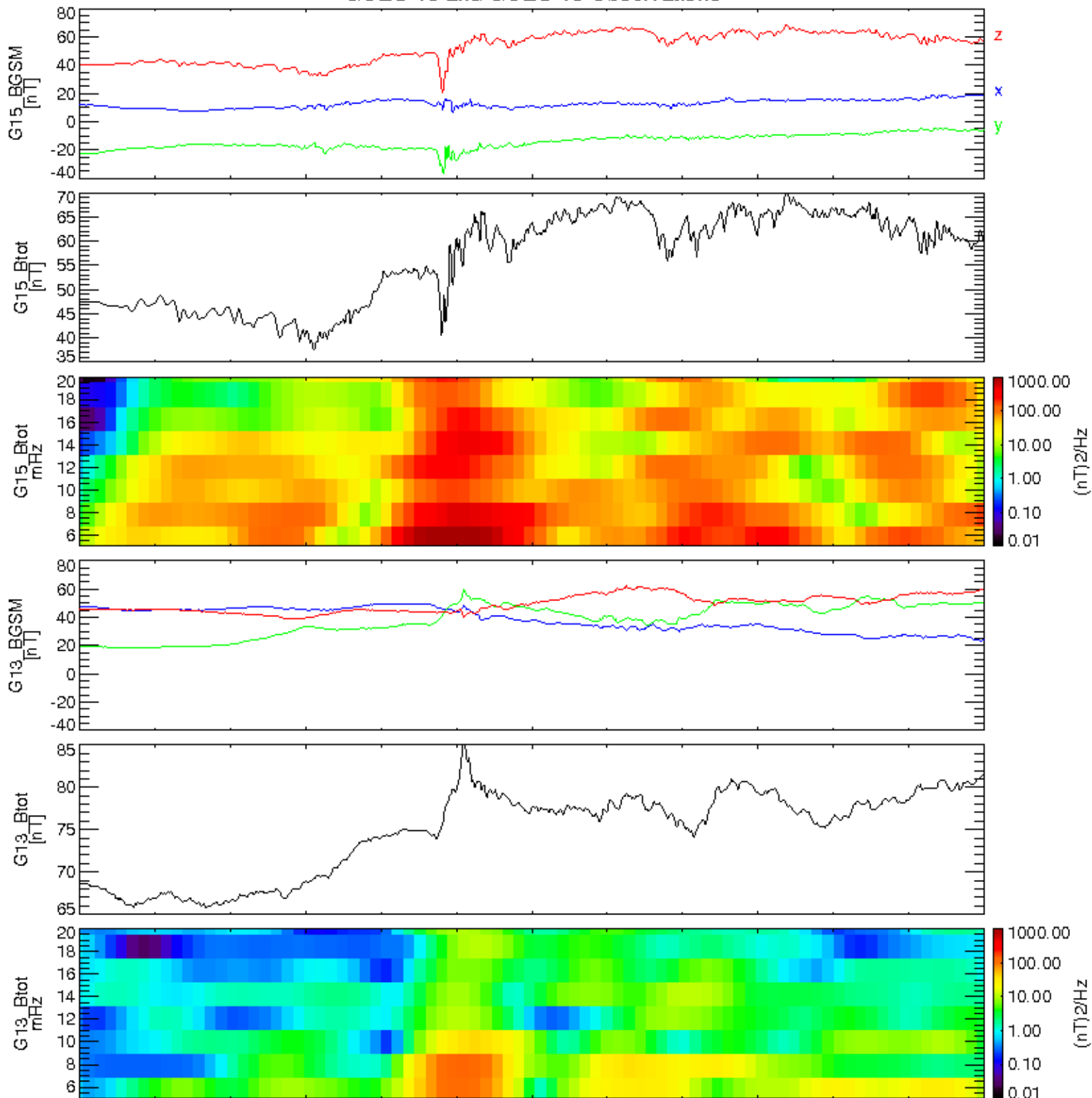


hh mm
2013 Mar 16

This article is protected by copyright. All rights reserved.

Author Manuscript

GOES-15 and GOES-13 Observations

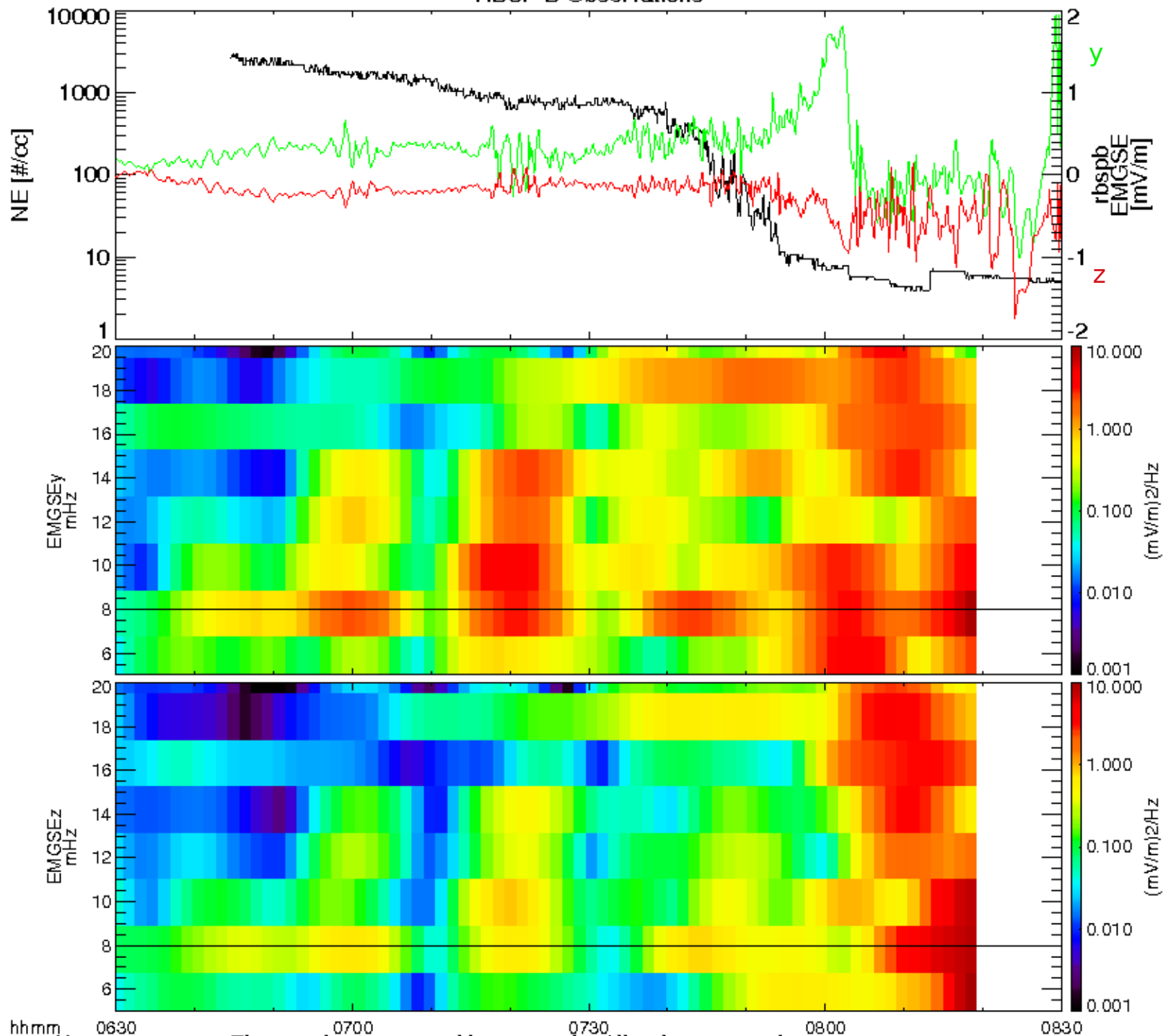


hhmm 0630
2013 Mar 16

0700 0730 0800 0830
This article is protected by copyright. All rights reserved.

Author Manuscript

RBSP-B Observations



hhmm 0630
2013 Mar 16

This article is protected by copyright. All rights reserved.